On the in situ encapsulation of $MoSi_2B$ healing particles in YSZ TBCs

Self-healing of thermal barrier coating (TBC)

Irsandi Kurniadi Isnu

4415108

Materials Science and Engineering
Mechanical, Maritime and Materials Engineering (3ME)

TU Delft

On the in situ encapsulation of $MoSi_2B$ healing particles in YSZ TBCs

Self-healing of thermal barrier coatings (TBCs)

By

Irsandi Kurniadi Isnu

(Student number: 4415108)

in partial fulfilment of the requirements for the degree of

Master of Science
in Materials Science and Engineering

at the Delft University of Technology,
to be defended publicly on September 29th, 2016

Thesis committees:	Dr. Ir. W. G. Sloof	TU Delft, supervisor
	A. L. Carabat	TU Delft
	Dr. S. R. Turteltaub	TU Delft
	Dr. T. Osada	NIMS, Japan

TU Delft

Abstract

A novel method to encapsulate $MoSi_2B$ healing particles was explored via in situ shell formation in yttria-stabilised zirconia thermal barrier coatings (YSZ-BCs). The shell formation was analysed for $MoSi_2B$ healing particles alloyed with 2, 6 and 12 wt% Al. According to oxidation kinetics study at 1100˚C using thermogravimetry, $MoSi_2B$-12 wt% Al particles formed exclusive alumina formation via selective oxidation of Al due to the more homogeneous distribution of $Mo(Si_{1-x},Al_x)_2$ among the particles. A more exclusive alumina formation was also favoured by oxidation in lower pO_2 using CO/CO_2 (ratio of 4.2, pO_2 of $9.1x10^{-14}$ atm) compared to oxidation in pure Argon. The shell formation of the Al-alloyed $MoSi_2B$ particles inside YSZ matrix composite was also studied. However, oxidation of composite containing $MoSi_2B$-12 wt% Al in the CO/CO_2 resulted in simultaneous oxidation of Al and Si with mixed silica-alumina was formed. This suggests zirconia matrix may play a role in oxidising the particles by partial reduction of YSZ. Nevertheless, shell showed protection for particles even after microcapsule stability test at 1100˚C in laboratory air for 100 hours. Crack-gap filling experiment was conducted for composites containing pre-encapsulated and in situ encapsulated $MoSi_2B$-6 wt% Al particles. Healing treatment was done with exposing the composites at 1100 ˚C for 1, 4 and 16 hours in laboratory air. However, the crack-gap was filled with silica without any significant difference.

Keywords: Self-healing, yttria stabilised zirconia, thermal barrier coatings, selective oxidation, in situ encapsulation, $Mo(Si_{1-x},Al_x)_2$ hexagonal C40, alumina

Preface

During the wonderful 2 years of my study at TU Delft, I have met many amazing people surrounding my life at TU Delft. I have been working on my thesis for the last 10 months and the beauty of experimental research is that it opens the opportunity to work directly or indirectly with others. I would like to send my biggest gratitude to Wim Sloof for letting me be involved in the project in the first place. The things I learnt from oxidation, self-healing, until on how being critical on my analysis have helped me becoming a better person and most importantly challenged my knowledge on materials science. Many thanks also to Alexandra Carabat who has been always a great help since the first day I started my thesis, as well as helping me with all the experiments and analysis. There are no words on how I much appreciate all the times spent for the favours and the countless discussion. Thank you also to Mario Ruiz and Toshio Osada for the many discussions. Working in a team definitely has helped me in to see a problem from different perspectives.

Without less respect, I would also like to express my gratitude to: Hans Brouwer who helped me with all the tools and equipment: SPS, furnace, TAG, and also for all the small-countless things. Kees Kwakernaak for training me to operate SEM and also the tons of analysis with EPMA. Richard Huizenga for the discussion of XRD analysis. To Lu Shen, Linda Boatemaa and Ann-Sophie Farle who helped me with the discussion of mass-gain analysis, crack-healing experiment as well as self-healing. To Guoping Bei who taught me Rietveld refinement using MAUD. To William Mao for lending us the controlled atmosphere furnace and the discussion. Last but not least to the amazing people of MSE/MEA class of 2014, who helped me get through hard and fun times together.

Finally, I would like to thank the members of examination who have invested their time evaluating my thesis.

Irsandi Kurniadi Isnu

Delft, September 2016

Content

List of Figures

List of Tables

1

Introduction

1.1 General introduction

Thermal Barrier Coating (TBC) is employed on metal or superalloy surface for its high-temperature resistance. Among many other, Yttria-stabilised Zirconia/YSZ (Y_2O_3-Stabilised ZrO_2) as Top Coat (TC) of the TBC is superior to other materials because it inherits low thermal conductivity, high CTE (~11 x 10^{-6}/°C) and resistant to hot corrosion[1, 2]. However, high temperature and prolong thermal cycling of TBC may induce crack. Cracks may be generated by the stress exerted by Thermal Growth Oxide (TGO) formation e.g. Al_2O_3, Cr_2O_3, and also by the thermal expansion mismatch with the layers underneath the TC. The initiation and propagation of this crack ultimately leads to failure of the coating.

In the structural application, self-healing of crack offers an interesting solution to prolong the lifetime of the coating. Autonomous healing in ceramic matrix composite has been observed before[3, 4]. Self-crack healing capability with 10-20 vol% SiC particles in ceramic composite has been found in alumina (Al_2O_3)[5], mullite ($3Al_2O_3.2SiO_2$)[6], silicon nitride (Si_3N_4)[7] and zirconia (ZrO_2)[8] ceramic matrix. The crack exposes the particles to air and eventually leads to oxidation. The oxidation product SiO_2 has almost two times larger molar volume compared to the initial particle. This newly provided bonded-material on the crack wake administers the autonomous strength recovery of the matrix.

Among any other silicon containing intermetallic materials, WSi_2 and $MoSi_2$ (CTE of around 8.5x10^{-6}/°C[9]) has comparable thermal expansion with ZrO_2 (CTE of 9 x 10^{-6} /°C[10]). Meeting this requirement, these materials thus are applicable as healing particles in YSZ-TBC system[11]. Upon oxidation, amorphous silica (a-SiO_2, Vm of 27.3 cm^3) is formed, and may react with tetragonal ZrO_2 matrix (t-ZrO_2, Vm of 20.4 cm^3)[12] by the dissolution of Si^{4+} in ZrO_2 forming zircon ($ZrSiO_4$, Vm of 38.7 cm^3)[13]. It has been observed crack healing in YSZ with B-doped $MoSi_2$ formed B-doped a-SiO_2 oxide (borosilicate) and crack far from the healing particles was filled[14]. Third element such as B offers low viscosity SiO_2/B_2O_3 glassy oxide[15,

[16]. C/SiC composite containing multilayer of boron-species (BN, B_4C, or SiBC) formed low-viscosity B_2O_3 oxide glass at low temperature oxidation (650 °C<T<900 °C) filling the porous of the composite[17]. Whereas at higher temperature (T > 900 °C), oxide glass of borosilicate heals the crack. Both glassy oxides have a low viscosity and therefore are vitreous to fill the crack/porous present in the matrix; see **Figure 1.1** for the self-healing schematic of YSZ-TBC. Due to the oxygen transparency in zirconia-based materials as the matrix ($D = 10^{-9} – 10^{-10}$ m^2/s at 1423 K and activation energy of ~1.0 eV)[9], $MoSi_2$ is easily oxidised even in the absence of crack. This premature oxidation without the presence of crack generates stress by the volume expansion and eventually the failure of TBC system. A protecting shell of the healing particles with low oxygen permeability is thus necessary.

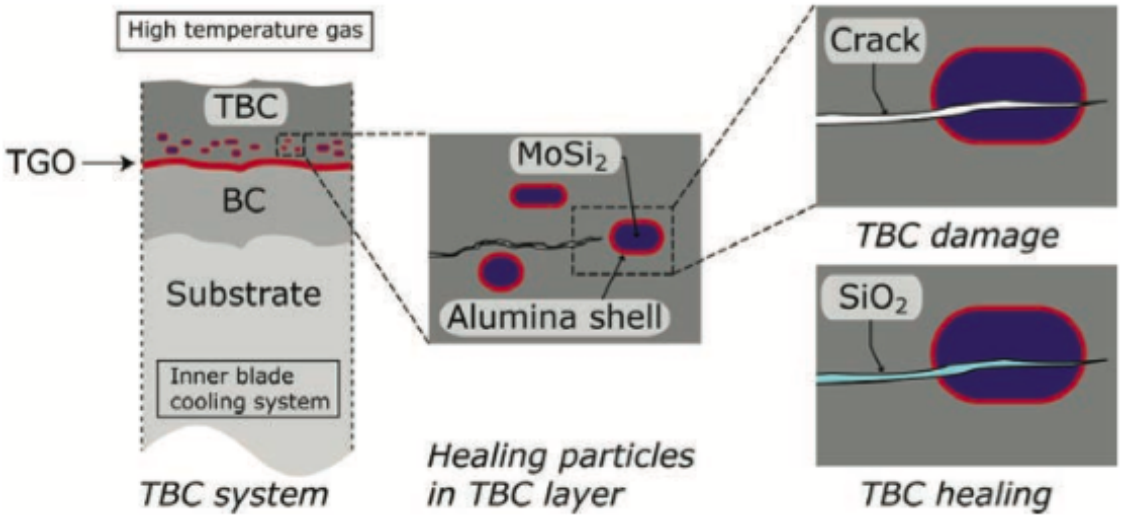

Figure 1.1: Schematic of self-healing mechanism in YSZ-TBC with alumina-encapsulated $MoSi_2$ healing particles[11].

The importance of microcapsule to prevent premature release of reactive agent has been underlined in self-healing system of polymer[18]. However, a polymer microcapsule is not stable in high-temperature application. At operating temperatures of TBCs, ceramic oxide such as Al_2O_3 is an interesting protection shell due to its low oxygen diffusivity ($D = 2 \times 10^{-24}$ m^2/s at T = 1423 K)[19]. There are several methodologies of alumina coating on particles: pure route[20], atomization[21], and wet route[22]. Moreover, $MoSi_2B$ healing particles has also been studied before. Carabat et al. encapsulated $MoSi_2$ by 150 nm thickness of α-Al_2O_3 by the transformation from γ → δ → Θ → α phase with two step annealing process of boehmite (AlOOH) sol-gel[23]. The Al_2O_3-encapsulated $MoSi_2$ showed much more oxidation resistant than the non-encapsulated particles. In some of sacrificial particles, a more oxygen-protective shell of aluminosilicate phases such as mullite ($3Al_2O_3.2SiO_2$, $D = 10^{-20}$ m^2/s at 1500 - 1725

K) was also formed. Encapsulation of $MoSi_2$ with Al_2O_3 via Atomic Layer Deposition (ALD) was also conducted even though the alumina phase transformation was different with those in sol-gel method[24]. In ALD, liquid trimethylaluminium (TMA) was used as the aluminium precursor. However, both sol-gel and ALD method promotes a thin alumina shell (150 nm). These pre-encapsulated $MoSi_2$ particles are then to be incorporated to YSZ matrix. A new method to encapsulate $MoSi_2$ with thicker shell is thus required.

In this thesis, a novel encapsulation method of $MoSi_2B$ healing particles with alumina shell is proposed. Instead of pre-encapsulating the particles, alumina shell growth is induced in situ inside the YSZ matrix through the selective oxidation of Al that is alloyed to $MoSi_2B$ particles. To this end, the composite of YSZ matrix with Al-alloyed $MoSi_2B$ particles was made by Spark Plasma Sintering (SPS). The growth of alumina shell is promoted by careful low pO_2 annealing to selectively oxidise Al. In situ encapsulation by using Al-alloyed $MoSi_2B$ particles showed successful alumina shell formation protecting the particles from premature oxidation.

1.2 Outline of the thesis

In this thesis, new approach to promote a protective shell around $MoSi_2B$ with protective shell is proposed. Chapter 1 addresses the necessity and the importance to develop new encapsulation method for $MoSi_2B$ healing particles. In chapter 2, the theoretical background of YSZ as well as oxidation of $MoSi_2$, B-alloyed $MoSi_2$ and Al-alloyed $MoSi_2$ are described as they underline the fundamental of Al depletion during oxidation. Details of the materials, experimental methods and characterisation techniques are presented in chapter 3. Three main studies were performed: oxidation kinetics of Al-alloyed $MoSi_2B$ powders, in situ Al_2O_3-encapsulation of Al-alloyed $MoSi_2B$ particles inside YSZ matrix, and crack-gap filling experiment. Oxidation kinetics of self-healing particles is designated to study the oxide growth in low pO_2 atmosphere. The oxide formation was then studied for composite containing YSZ matrix and Al-alloyed $MoSi_2B$ healing particles. After the in situ encapsulation of $MoSi_2B$ healing particles, the composite undergoes microcapsule stability test by exposing it at 1100 °C air for 100 hours in laboratory air. Cracks are also introduced with indentation and then healed through oxidation in air to study the crack-gap filling. Chapter 4 and 5 address the results and discussion, respectively. Finally, the conclusions and proposed recommendations for future work will be presented in chapter 6.

2

Theoretical Background

2.1 $MoSi_2$

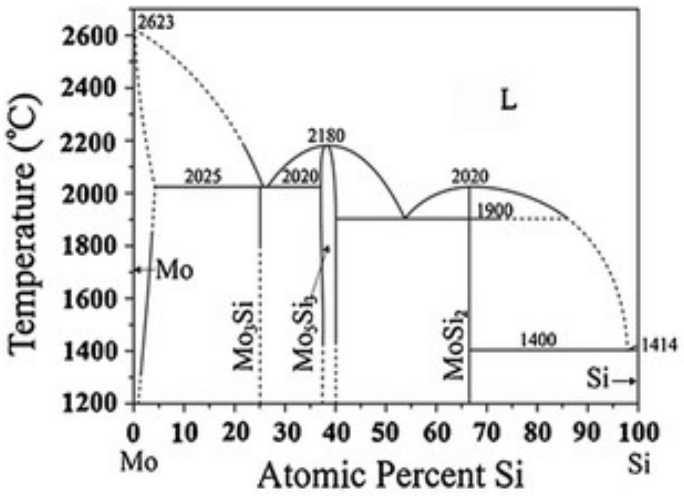

Figure 2.1: Phase diagram of Mo-Si system[25].

Due to its high melting temperature (2030 ºC), molybdenum disilicide ($MoSi_2$) intermetallic is beneficial for high temperature application. **Figure 2.1** illustrates the binary phase diagram of Mo-Si system[25]. At lower temperature (T < 800 °C), Si self-diffusion is very slow thus Mo and Si are oxidised simultaneously as shown in reaction **(2.2**). Cracks are generated due to the molar volume is increased by 250% upon the formation of needle like MoO_3 and $MoO_3{\cdot}2SiO_2$. The disintegration caused by this MoO_3 formation is called pest oxidation[26, 27].

$$\frac{5}{7}MoSi_2 + O_2 \rightarrow \frac{1}{7}Mo_5Si_3 + SiO_2 \qquad \textbf{(2.1)}$$

$$\frac{2}{7}MoSi_2 + O_2 \rightarrow \frac{2}{7}MoO_3 + \frac{4}{7}SiO_2 \qquad \textbf{(2.2)}$$

At high temperature (T ≥ 1000 ºC), oxidation reaction **(2.1)** is more favourable as it has higher absolute value of Gibbs free energy per 1 mole of O_2[28, 29]. As Si is consumed, a

Si-depleted zone of Mo_5Si_3 (D8m crystal structure) is formed, i.e. between the bulk $MoSi_2$ and silica layer. It is important to note as well that Mo_5Si_3 was not always present in all studies which might be due to the volatilisation of Mo oxidation product[30, 31]. If the silica film is thick and continuous, the low pO_2 between the silica film and bulk Mo-Si prevent MoO_3 formation, therefore oxidation of Si becomes selective. Also, at these temperatures the Si self-diffusion in $MoSi_2$ is higher compare to Mo. After the protective silica is formed, the rate-limiting step of oxide formation is the diffusion of O_2 molecules through the silica layer. The drawback of silica protective oxide scale is that it is crystallized to tridymite at 1000-1200 °C and to β-cristobalite at 1300-1400 °C[27] and then to α-cristobalite during cooling to T=540 K accompanied with volume change[31]. This volume change could result in crack and spallation. Sharif et al. measured that the high order of crystal silica also lowered the activation energy of oxygen diffusion and thus rapid oxidation was occurred[32]. SiO_2 suffers also from volatilisation of $SiO_{(g)}$ and $SiO_{2(g)}$ during oxidation at very high temperature (1600-2000 K) or at very low pO_2 ($<10^{-8}$ atm).

2.2 B-alloyed $MoSi_2$

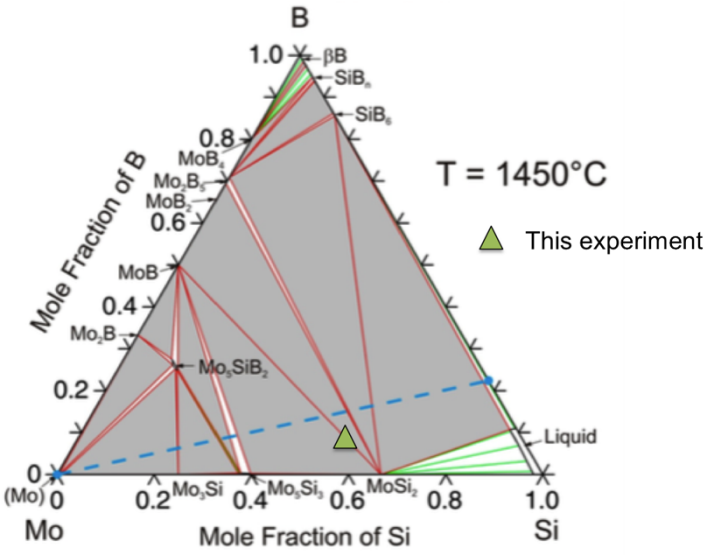

Figure 2.2: Phase Diagram of Mo-Si-B system at T=1450 °C [33].

A few studies have been conducted to observe the oxidation behaviour of Mo-Si-B alloys usually with rich-Mo alloys. Paswan et al. observed the protective B_2O_3-SiO_2 (B-doped silica) scale formed at 1150 °C. The alloy was fabricated with composition of high Mo (~76 at% Mo) and small amount of Si (~14 at% Si) and B (8-10 at% B). The small amount of B incorporated the silica resulted in glassy-like scale. Supatarawanich et al. studied the Mo-Si-B alloy and found at intermediate temperature oxidation the B-doped silica glass was formed

from the oxidation of Mo_5SiB_2 with T2 crystal structure[34]. In the case of B-modified $MoSi_2$ coating, Tian et al. found the viscous B_2O_3-SiO_2 oxide filled porosity of the scale preventing further MoO_3 volatilisation.

According to Ingemarsson et al., oxidising $Mo(W,Si)_2$ with boride (10-12 vol% B) at high temperature results in two layer oxide, boron-rich silica on the outer side and boron-poor silica beneath it[35]. The mixture of B_2O_3/SiO_2 yields a borosilicate phase of glass since B_2O_3 is known to dissolve into SiO_2. Borosilicate glass is a type of glass consisting of SiO_2-B_2O_3-Na_2O system which lower viscosity at any temperature compared to silica glass[36]. B_2O_3 creates 2D connectivity with SiO_4 tetrahedra network that eventually decreases the rigidity of the glass[37]. Such elements that are able to influence the structure and property of glass/melts are referred as glass-modifying oxides alkali and alkaline earths. Lower viscosity of borosilicate glass was also confirmed by other research as well[38, 39].

2.3 Al-alloyed $MoSi_2$

SiO_2 may also suffer from pest disintegration and SiO volatilization at low pO_2. Metals with higher affinity to oxygen (such as Al, Ta and Ge) are usually alloyed to $MoSi_2$ to overcome the problem that arises from a SiO_2 oxide scale[26, 40]. Due to the large negative Gibbs free energy of formation at high temperatures, Al_2O_3 is preferentially formed instead of SiO_2[41]. Al_2O_3 scale offers protection against pest disintegration and it has lower oxide volume expansion compared to SiO_2, which are 4.9% and 85.6% respectively[42, 43].

The phase diagram of Mo-Al-Si system has been assessed[44-46] as shown in **Figure 2.3**. $MoSi_2$ with tetragonal $C11_b$ (space group *I4/mmm*) crystal structure has a limited Al solubility (<5 mol% Al)[47]. $Mo(Al_x,Si_{1-x})_2$ with hexagonal with C40 (space group $P6_222$) crystal structure is formed when more Al is doped exceeding the solubility limit of tetragonal $C11_b$. Dasgupta et al. studied the synthesize of $Mo(Al_x,Si_{1-x})_2$ alloy by arc-melting of the stoichiometric amount of Al-Si eutectic alloy and high-purity Mo powders[48]. They found that hexagonal C40 phase did not form unless x reached 0.05. The hexagonal C40 phase has the advantage of its higher Al solubility ($0.11 < x < 0.55$) and wider ratio of Al substitution to Si[49]. They concluded by adding more Al increases the lattice parameter of tetragonal $C11_b$ since al has larger atomic radius (143 pm) than Si (117 pm), which consequently increases the *d* value and its molar volume[50].

The oxidation behaviour of $Mo(Al_x,Si_{1-x})_2$ has been studied for its good oxidation resistance in high temperature application. In the range of 1273-1873 K, the scale consisted mainly of α-Al_2O_3. However depending on the Al activity and temperature, amorphous silica and aluminosilicate such as mullite ($3Al_2O_3.2SiO_2$) may be present as well. Stergiou et al.

observed that addition of Al x = 0.33 and x = 0.44 increases the resistance against pest oxidation[30]. An oxide scale consisted of α-Al_2O_3 was found when oxidizing $Mo(Si_{1-x},Al_x)_2$ with x = 0.33 and x = 0.44 in air at 1623 K. Below this temperature, both of these alloys formed Al-Si mixed oxide instead. Mitra et al. suggested that the oxidation rate was increased for $Mo(Al_x,Si_{1-x})_2$ compared to $MoSi_2$ due to the rapid depletion of Al[43]. Similarly, Ramberg et al. investigated the difference of oxide between $Mo(Al_{0.01},Si_{0.99})_2$ and $Mo(Al_{0.1},Si_{0.9})_2$ alloys[51]. At temperature above 1000 °C, the main oxide scale of $Mo(Al_{0.01},Si_{0.99})_2$ alloy is composed of amorphous silica, mullite, sillimanite (Al_2SiO_5), and even cristobalite after long and high-temperature exposure. On the contrary, $Mo(Al_{0.1},Si_{0.9})_2$ oxidation consisted mainly of alumina. After oxidation, Al depleted region-Mo_5Si_3 beneath the scale was found for $Mo(Al_{0.01},Si_{0.99})_2$ but not for $Mo(Al_{0.1},Si_{0.9})_2$. Although the Al content of the alloy was unknown, the existence of the Al-depleted Mo_5Si_3 region was also confirmed by Ingemarsson et al when using $Mo(Si,Al)_2$-based composite from Kanthal Super ER from Sandvik Heating Technology[31, 52]. In their study, they found continuous protective alumina oxide scale and the thickness of the scale is two times thicker than the oxide formed on Al-free $MoSi_2$ material.

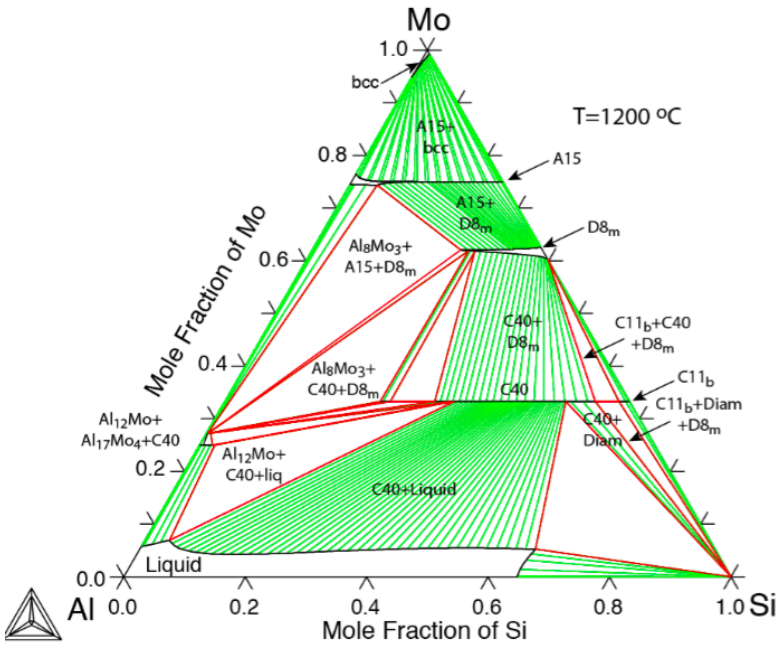

Figure 2.3: Phase diagram of Mo-Al-Si system at T=1200 °C [53].

2.4 Yttria-stabilised zirconia

Zirconia (ZrO_2) inherits low thermal conductivity, high strength and good chemical resistance properties that make the material beneficial for structural applications in harsh and high-loading condition. Zirconia is polymorph that consists of three phases: room

temperature monoclinic m-ZrO_2, at higher temperatures tetragonal t-ZrO_2 (950-1150 °C) and at very high temperatures cubic c-ZrO_2 (2300±30 °C). Pure zirconia is detrimental due to the martensitic transformation with 8 vol.% changes during t-ZrO_2 ↔ m-ZrO_2. To prevent this martensitic transformation, stabilisers such as yttria (see **Figure 2.4**), calcia, magnesia and rare earth oxide are doped to zirconia to stabilise t-ZrO_2 or c-ZrO_2 at room temperature[54].

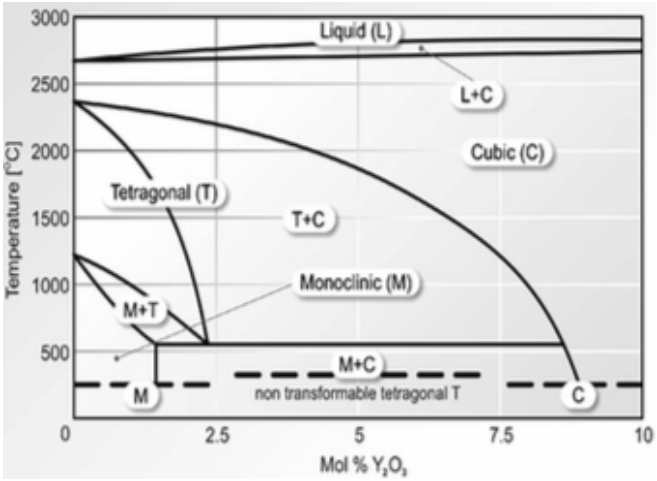

Figure 2.4: Phase diagram of ZrO_2-Y_2O_3 system[55].

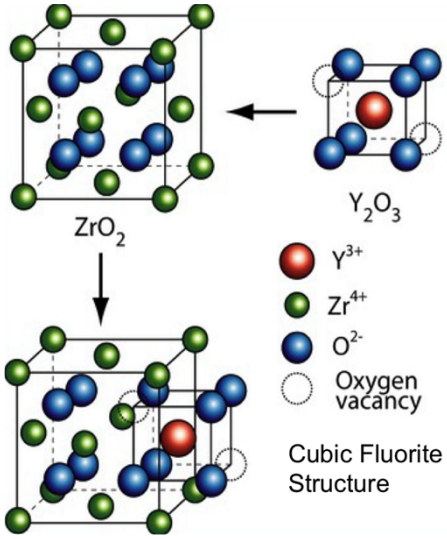

Figure 2.5: Schematic of $V\ddot{o}$ formation by Y_2O_3 doping to ZrO_2.

Doping Yttria (Y_2O_3) to zirconia facilitated by substitution of Zr^{4+} with Y^{3+} introduces oxygen vacancies to the lattice to maintain charge neutrality,

$$Y_2O_3 \rightarrow 2Y'_{Zr} + 3O_o^x + V\ddot{o} \qquad \textbf{(2.3)}$$

The incorporation of oxygen vacancies $V\ddot{o}$ (see also **Figure 2.5**) into the lattice raises the high oxygen conductivity of yttria-stabilised zirconia (YSZ). Depending on the yttria content, the stabilised zirconia phases may be different. With addition of 3 mol% Y_2O_3, zirconia is partially stabilised zirconia (PSZ) and it is comprised of t-ZrO_2/c-ZrO_2 and m-ZrO_2[56]. About 6-8 wt% (3-5 mol%) addition of Y_2O_3, metastable tetragonal t'-ZrO_2 may be precipitated in a rapid cooled YSZ (e.g. as in plasma sprayed YSZ)[57, 58]. On the other hand, fully stabilised zirconia (FSZ) is comprised only t-ZrO_2/c-ZrO_2 with the addition of 8-10 mol% Y_2O_3.

3

Materials and Experimental Methods

3.1 Starting materials

3.1.1 Preparation of powders

3 mol% Yttria Stabilised Zirconia (YSZ) powders (Tosoh, Japan) were used as the matrix in the composite. The healing particles, Al-alloyed $MoSi_2B$ (2 wt% B-doped $MoSi_2$) powders supplied by Chempur (see **Table 3.1**). Wind-sifting with an Alpine 100 MRZ laboratory zig-zag classifier was conducted to eliminate fine fraction and to obtain a sharper particle size distribution. The target content of Al doping of $MoSi_2B$ was varied from 2, 6 and 12 wt% Al, which from here and onwards will be denoted as $MoSi_2B$-2 wt% Al, $MoSi_2B$-6 wt% Al, $MoSi_2B$-6 wt% Al and $MoSi_2B$-12 wt% Al, respectively. X-Ray Fluorescence (XRF) and X-Ray Diffractometry (XRD) were performed to analyse the composition of the powders. Scanning Electron Microscope (SEM) combined with Energy Dispersive X-Ray Spectroscopy EDS) and Electron Probe X-Ray Micro Analysis (EPMA) were also employed to analyse the chemical composition. However, $MoSi_2B$-2 wt% Al powders were only investigated with XRD.

Table 3.1: Denotations of the composite samples: YSZ matrix with 10 vol% of Al-alloyed $MoSi_2B$ particles (YSZ+10MBSA).

Matrix	Healing particles	YSZ+10MSBA Composite
3YSZ	$MoSi_2B$-2 wt% Al	YSZ+10MSB2A
	$MoSi_2B$-6 wt% Al	YSZ+10MSB6A
	$MoSi_2B$-12 wt% Al	YSZ+10MSB12A

3.1.2 Oxidation study

Thermogravimetry Analysis (TGA) was performed to study the oxidation of $MoSi_2B$-6 wt% Al and $MoSi_2B$-12 wt% Al particles using a high precision balance and high precision dual furnace (TAG Setaram Instrumentation, France). The mass change with time during isothermal annealing at 1100˚C for 48 hours is observed. Alumina crucibles were used for sample powders and also for reference (empty-crucible). A micro-balance (Mettler

Instrumente AG CH-8606, USA) with accuracy of 10^{-6} g was used to measure the weight the mass of the powders used in the TGA experiment. The set of powders and the annealing condition are detailed in **Table 3.2**. Two different annealing atmospheres were used: pure Argon and CO/CO_2 (ratio of CO/CO_2 is 4.2, pO_2 = 9.1 x 10^{-14} atm, see **Table B.3.1**). CO/CO_2 was only flown during the isothermal annealing. Annealing at 200 °C for 30 minutes was designated to evaporate any water vapour and contaminants that may surface on the powders. The annealed powders were then analysed with SEM/EDS to investigate the oxide constituents.

Table 3.2: Samples and annealing profile for TGA experiment.

No	Powders	Gas flow (mL/min)	Annealing Profile				
			Cleaning temp (°C)	Time (h)	Annealing temp (°C)	Time (h)	Rate (°C/min)
1	$MoSi_2B$-6 wt% Al	Argon 50	200	0.5	1100	48	10
2	$MoSi_2B$-12 wt% Al						
3	$MoSi_2B$-6 wt% Al	16.8 CO + 4 CO_2 + 29.2 Argon (CO/CO_2 = 4.2)*					
4	$MoSi_2B$-12 wt% Al						

*Only flown during isothermal annealing for 48h

3.2 $MoSi_2$-in situ Alumina Encapsulation

3.2.1 Mixture of powder and sintering

The volume ratio of YSZ powders as matrix and Al-alloyed $MoSi_2B$ powders (YSZ+10MSBA) as the healing particles was 9:1 (10 vol% Al-alloyed $MoSi_2B$). The particles are Al-alloyed $MoSi_2B$ with Al varied from 2, 6 to 12 wt%. With these composition, three composites were prepared: YSZ+10MSB2A, YSZ+10MSB6A and YSZ+10MSB12A (**Table 3.1**). In a plastic bottle, the powder mixtures were then dispersed in C_3H_7OH (iso-propanol) and mixed using ZrO_2 balls (diameter of 5mm) with a powder to ZrO_2 ball ratio of 1:1 for 16 hours. To this end a tubular mixer (Turbula, Switzerland) was used. Subsequently the powders mixture was dried in an oven (Binder, Germany) at 100 °C overnight. Afterwards, the powders were passed through a sieve of 200 µm to obtain a homogeneous mixture. Afterwards, the sieved-powders were dried again in the oven at 100 °C to ensure no water vapour was stored inside the powder mixture.

The sintering of composites was done with Pulsed Electric Current Sintering or Spark Plasma Sintering/SPS (FCT Systeme GmbH, Germany). The schematic of SPS is shown in **Figure 3.1.** As zirconia is a highly insulating material, graphite paper (thickness of 0.18 mm)

was placed around the powders, forcing the DC current to go around the powders mixture and allowing joule heating to take place. The operating parameters for the sintering are listed in **Table 3.3**. The system was flushed with pure Argon and then evacuated repeatedly prior to sintering process to remove the remaining oxygen and water molecules that might reside inside the chamber. The powders were also pre-pressed with force of 5 kN in this stage. After 30 minutes of sintering at 1200 °C, the pistons and punches were released from the sintered sample allowing natural cooling. After the sintering, the graphite around the sample was removed with coarse SiC grinding paper.

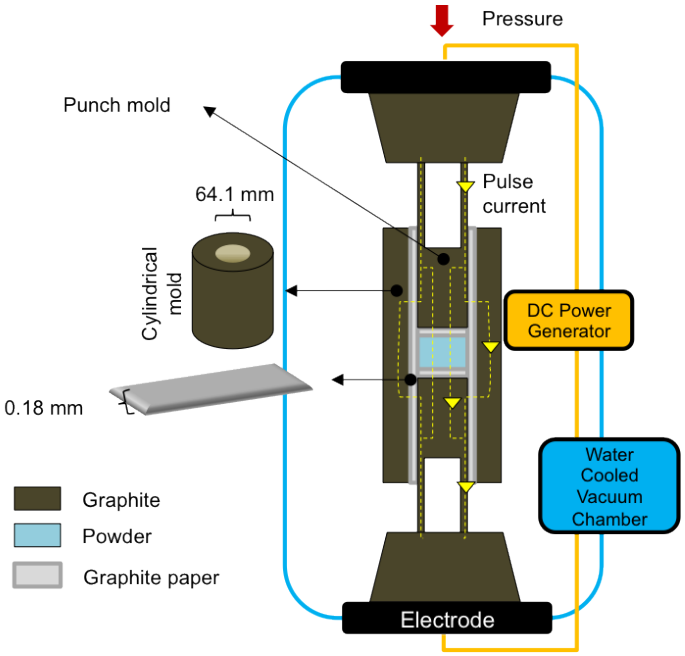

Figure 3.1: Schematic of Spark Plasma Sintering (SPS).

Table 3.3: Spark Plasma Sintering (SPS) operating parameters.

Parameter	Set value
Current	5 kA
Voltage	5 V
Pre-press	5 kN
Pressure	16 kN
Atmosphere	Ar
Power	65% power limit
5V pulse time	15 µs
5V pause time	5 µs
Pre-press	5 kN
Heating rate	20 °C /min
Cooling	Natural cooling

3.2.2 Annealing: aluminium depletion and microcapsule stability test

Two different annealing processes were performed with different objectives (see **Table 3.4** for specification of the annealing parameters). Low pO_2 annealing inside alumina tube furnace (Carbolite, Sigma-Aldrich, USA) is designated to create α-Al_2O_3 shell around the particles in the composite. Two different atmosphere of low pO_2 was used: pure Argon and CO/CO_2 (ratio of CO/CO_2 is 4.2, pO_2 = 9.1 x 10^{-14} atm at 1100°C, see **Table B.3.1**). Argon, CO and CO_2 gas was passed through O_2, H_2O and hydrocarbon filter (Kleinpatrone Aplhagaz, air Liquide, Germany) to remove the contaminants from the gas source. For the annealing in pure Argon, the system had been flushed first with Argon gas flow of 500 mL/min for 0.5-1 hour. Afterwards, the sample was exposed directly at 1100 °C for the annealing process. The sample was removed from 1100 °C heating zone and quenched with 500 mL/min Argon

gas. However, in the case of annealing in CO/CO_2, the samples were heated and cooled down with rate of 10 °C/min.

Table 3.4: Annealing parameters of low pO_2 annealing in Argon and CO/CO_2 (with ratio of 4.2) as well as parameters for microcapsule stability test.

Parameter	Parameters of Annealing		
	Al depletion in Argon	**Al depletion in CO/CO_2***	**Microcapsule Stability**
Annealing temperature	1100 °C	1100 °C	1100 °C
Holding annealing time	16 h	16 h	100 h
Gas flow	500 mL/min High-Purity Argon gas	448 Ar + 42 CO + 10 CO_2 (mL/min)	Open air
Heating and Cooling	Quench	Heating and Cooling rate 10 °C/min	Quench in air
Boat and substrate	Quartz boat and Silicon wafer	Quartz boat and Silicon wafer	Alumina boat
Tube	Alumina tube	Alumina tube	Quartz tube

*Experiment was only performed for YSZ+10MSB6A and YSZ+10MSB12A composite, not for YSZ+10MSB2A composite.

Microcapsule stability test was performed in an open alumina tube furnace (Carbolite, Sigma-Aldrich, USA) to check the stability of $MoSi_2B$ particles that had been encapsulated at 1100 °C for 100 hours in laboratory air. In between the total of 100 hours of annealing, the sample was taken out shortly to check the integrity of the sample.

3.3 Crack-gap filing

Composite containing YSZ matrix with pre-encapsulated and in situ encapsulated $MoSi_2B$-6 wt% Al (YSZ+10MSB6A) healing particles were investigated for crack-gap filling experiment. Details of pre-encapsulation process of the healing particles is discussed somewhere else[23, 24]. Crack was created with indentation (Zwick Hardness Tester, Germany) using diamond and pyramid-shaped indenter (136° between opposite faces). The load was selected between 200 N and 300 N. Afterwards the healing treatment was done by exposing the composites directly at 1100 °C in laboratory air using an alumina tube furnace and followed by quenched. The healing time was varied from 1, 4 and 16 hours for pre-encapsulated particles and only healed for 4 hours for the in situ encapsulated particles. The parameters for composite fabrication for both composites were the same as discussed in **Section 3.2.1** for SPS and **Section 3.2.2** for low pO_2 annealing.

3.4 Characterisation

A laser diffraction particle size analyser instrument (SDC Microtac S3500, USA) was used to obtain the particle size distribution of Al-alloyed $MoSi_2B$ and YSZ powders. X-Ray Diffraction/XRD (Bruker D8 Advance diffractometer, USA) was used for analysing the chemical composition of the sample. Bruker D8 was installed with Bragg-Brentano and Lynxexe position sensitive detector, and monochromatic Cu-Kα radiation. The XRD patterns were analysed using Rietveld refinement with Java program of MAUD (copyright of Luca Lutterorri, University of Trento, Italy). The elemental analysis of the powders was performed using X-Ray Fluoroscence (XRF) spectrometer (Panalytical Axios Max-WD, The Netherlands) and SuperQ5.0i/Omnian for XRF data evaluation.

The surface morphology and local chemical composition analysis was performed with Scanning Electron Microscope (SEM, JEOL 6500FD, Japan) equipped with a ThermoFisher Ultra Dry Energy Dispersive System (EDS). With SEM, two mode of imaging can be used; secondary electrons imaging (SEI) and backscattered electrons imaging (BEI). In case of the cross-section analysis with SEM/EDS, the sample was cut with diamond wafering blade (Isomet diamond blade, USA). A smooth surface was prepared with by grinding down to 2500 grit SiC paper and polishing down to 0.25 µm paste on a polishing cloth. As for investigation of powders, the powders were embedded in a conductive polymer (Technovit 5000, Germany) based on modified methyl methacrylate with dendritic copper particles. Cross-section of the powders was also done with the grinding and polishing of the embedded powders; see above. Prior to SEM/EDS analysis, embedded powders were cleaned with C_3H_7OH (isopropanol), whereas the composites were cleaned with both $(CH_3)_2CO$ (acetone) and isopropanol in ultrasonic bath (Branson 2510, Sigma-Aldrich, USA). After the cleaning, the samples were coated with carbon using an Auto-Carbon-Coater (JEOL JEC-530, Japan) with thickness of 10-15 nm. Electron Prove Micro-analyser (EPMA, JEOL JXA 8900R microprobe, Japan) was performed particularly for more accurate chemical composition analysis. In some cases, the samples were coated with carbon and silver to enhance the conductivity prior to EPMA investigation.

4

Results

4.1 Starting materials

4.1.1 Chemical composition and microstructure

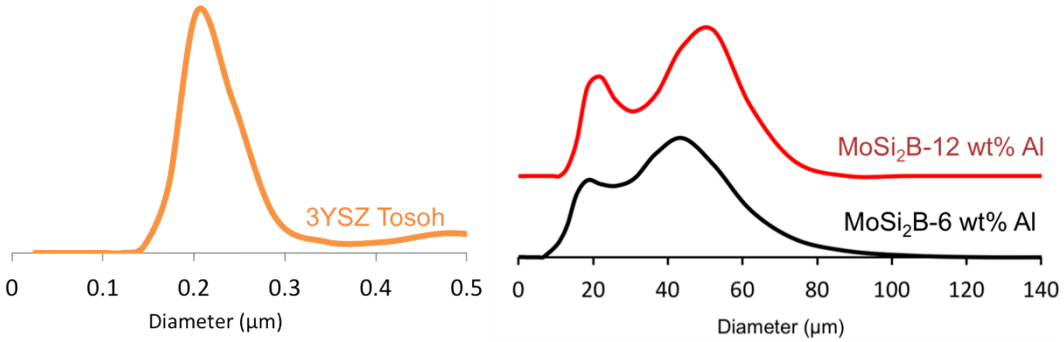

Figure 4.1: Particle size distribution of 3 mol% Y_2O_3-ZrO_2 (3YSZ) powders (left, orange line), as well as wind-sifted healing particles: $MoSi_2B$-6 wt% Al (right, black line) and $MoSi_2B$-12 wt% Al (right, red line).

Al-alloyed $MoSi_2B$ powders were wind-sifted to eliminate the fine fraction of the powders. However the particle size distribution for both $MoSi_2B$-6 wt% Al and $MoSi_2B$-12 wt% Al particles are still bimodal as seen in **Figure 4.1**. On the contrary, the particle size of YSZ powders is unimodal. The distribution values are tabulated in **Table 4.1**. Al-alloyed $MoSi_2B$ powders were also characterised with XRD (see **Table 4.2**) as well as with XRF and SEM/EDS (see **Table 4.3**, only for $MoSi_2B$-6 wt% Al and $MoSi_2B$-12 wt% Al). The XRD shows mainly $Mo(Al_x,Si_{1-x})_2$ hexagonal C40 in $MoSi_2B$-12 wt% Al with very small fraction of $MoSi_2$ tetragonal $C11_b$. However, there is a co-existence with tetragonal $C11_b$ in $MoSi_2B$-6 wt% Al. **Table 4.4** shows the weight fraction of tetragonal $C11_b$ and hexagonal C40 for $MoSi_2B$-6 wt% Al and $MoSi_2B$-12 wt% Al powders in the starting condition and after oxidation (oxidation kinetics of $MoSi_2B$-6 wt% Al and $MoSi_2B$-12 wt% Al is discussed in **Section 4.1.2** using Rietveld refinement in the 2θ range of 0-35.5° (see **Table A.2.1** for the complete result). The peak position in the diffractograms for both hexagonal C40 and tetragonal $C11_b$ between $MoSi_2B$-6 wt% Al and $MoSi_2B$-12 wt% Al are shifted without peak broadening (see

Figure 4.2). Beside the dominant peaks of hexagonal C40 and tetragonal $C11_b$, Mo_5Si_3 and signal corresponding to Al and Si are detected as well. Other considerably high peaks (0.2-7.6 wt%) are corresponded to Mo-B phases: MoB, MoB_2 and Mo_2B_5. The chemical composition of 3YSZ powders was taken from manufacturer data and is shown in **Table 4.2**.

Table 4.1: Particle size distribution for starting powders.

Parameter	Wind-sifted $MoSi_2B$-6 wt% Al (µm)	Wind-sifted $MoSi_2B$-12 wt% Al (µm)	3YSZ Tosoh (µm)
D[10]	13.4	16.7	0.2
D[50]	29.9	34.6	0.2
D[90]	52.8	56.3	0.4

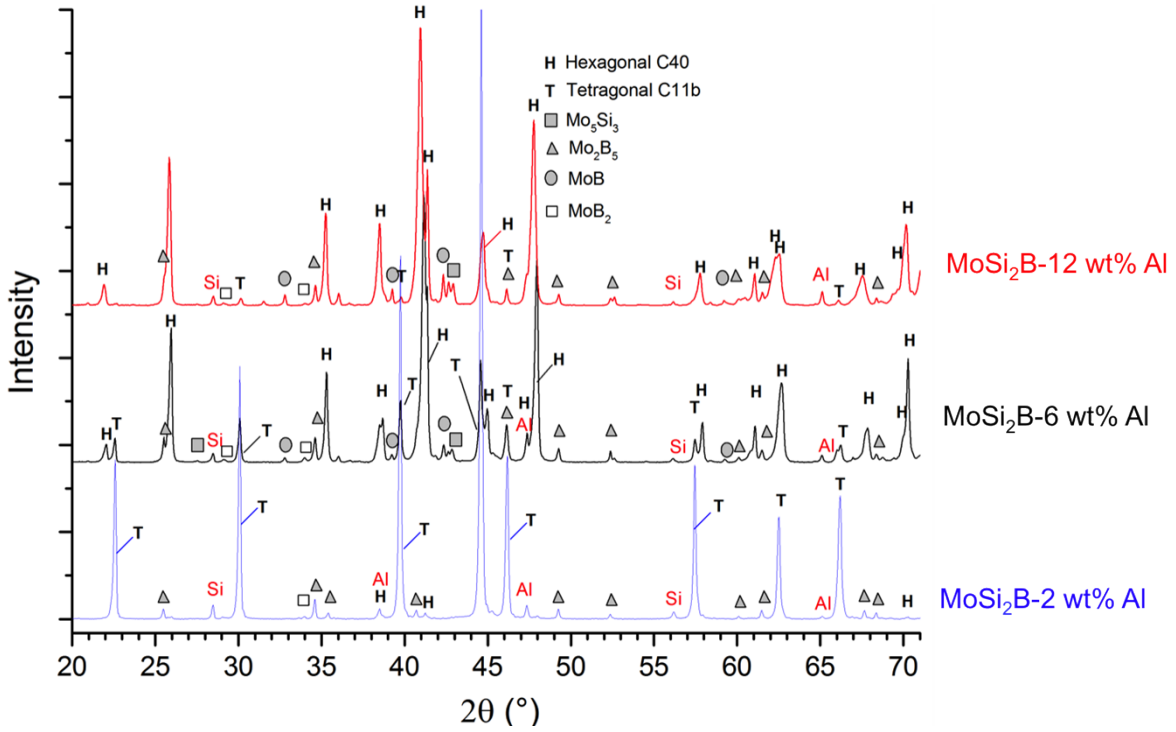

Figure 4.2: X-Ray Diffraction (XRD) of starting $MoSi_2B$-2 wt% Al, $MoSi_2B$-6 wt% Al and $MoSi_2B$-12 wt% Al powders.

Table 4.2: Main and impurities chemical composition of 3YSZ Tosoh powders (taken from manufacturer data).

3YSZ Tosoh	Y_2O_3	HfO_2	Al_2O_3	SiO_2	Fe_2O_3	Na_2O
wt%	5.2+0.5	<5.0	0.1-0.4	≤0.02	≤0.01	≤0.04

Table 4.3: Elemental analysis using XRF and EPMA of the starting $MoSi_2B$-6 wt% Al and $MoSi_2B$-12 wt% Al.

Analysis	Compound	$MoSi_2B$-6 wt% Al (at%)	$MoSi_2B$-12 wt% Al (at%)
XRF	Mo	43.9	39
	Si	41.8	34.4
	Al	14.1	26.4
	Fe	0.13	0.1
	Ca	0.07	0.08
	Cr	0.02	0.005
	Cu	0.01	0.01
EPMA	Al	$4.7^{+2.7}_{-3.5}$	$8.2^{+8.0}_{-3.0}$

$MoSi_2B$-6 wt% Al and $MoSi_2B$-12 wt% Al powders embedded in a conductive polymer were examined with SEM (See **Figure 4.3** for cross-section of $MoSi_2B$-6 wt% Al). According to SEM/EDX analysis, $MoSi_2B$-6 wt% Al and $MoSi_2B$-12 wt% Al particles consist of $Mo(Al_x,Si_{1-x})_2$, $MoSi_2$ and Mo_5Si_3 (with dissolved ~0.41 wt% Al in average inside Mo_5Si_3). Dark-spots of Al_2O_3 and SiO_2 impurities are also found in the starting Al-alloyed $MoSi_2B$ powders. It can be seen that the shape of particles is irregular. Statistical analysis using EPMA (**Table 4.3**) for many particles shows that the average Al content is $4.7^{+2.7}_{-3.5}$ at% Al and $8.2^{+8.0}_{-3.0}$ at% Al for $MoSi_2B$-6 wt% Al and $MoSi_2B$-12 wt% Al, respectively (1 Al atomic fraction/at% in $Mo(Al_x,Si_{1-x})_2$ is approximately equivalent to 2 Al in weight fraction/wt%). This suggests that the distribution of phases among particles is not homogeneous.

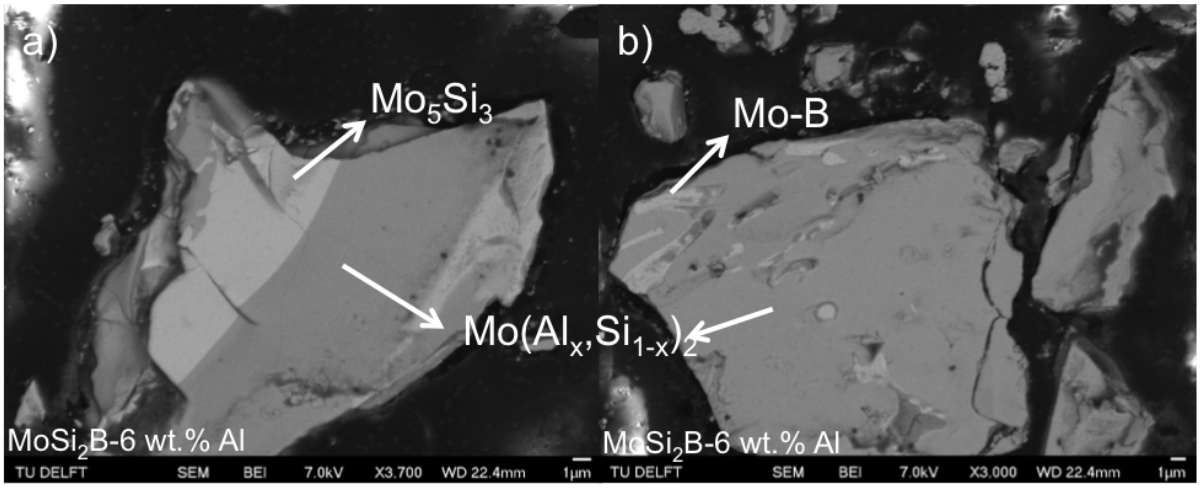

Figure 4.3: Cross-section of wind-sifted $MoSi_2B$-6 wt% Al powders.

4.1.2 Oxidation kinetics and microstructure

The mass gain ($\Delta m/m_o$) of $MoSi_2B$-6 wt% Al and $MoSi_2B$-12 wt% Al particles versus exposure time *t* of isothermal annealing at 1100 °C for 48 hours in Argon and CO/CO_2 is

shown in **Figure 4.4**. The mass-gain difference measured between TGA and the microbalance was of the order of 10^{-4}-10^{-5} gr, which is reasonable. The oxidation of $MoSi_2B$-6 wt% Al and $MoSi_2B$-12 wt% Al powders in pure Argon and CO/CO_2 have different mass-gain behaviour (See **Figure 4.4**). For oxidation in pure Argon, there are 3 runs for each Al-alloyed $MoSi_2B$ powders and the mass-gain is represented in area according to the vertical lines. In this environment, $MoSi_2B$-6 wt% Al has more mass-gain compared to $MoSi_2B$-12 wt% Al. Both of the particles inherit quite constant slope. Oxidation of Al-alloyed $MoSi_2B$ particles in CO/CO_2 results in more mass-gain compared to the oxidation in pure Argon. Contrary to oxidation in pure Argon, $MoSi_2B$-12 wt% Al has more mass-gain compared to $MoSi_2B$-6 wt% Al in CO/CO_2. Here, a steep mass-gain in the first few hours of oxidation clearly revealing the fast-initial oxidation stage which then followed by steady-state oxidation stage.

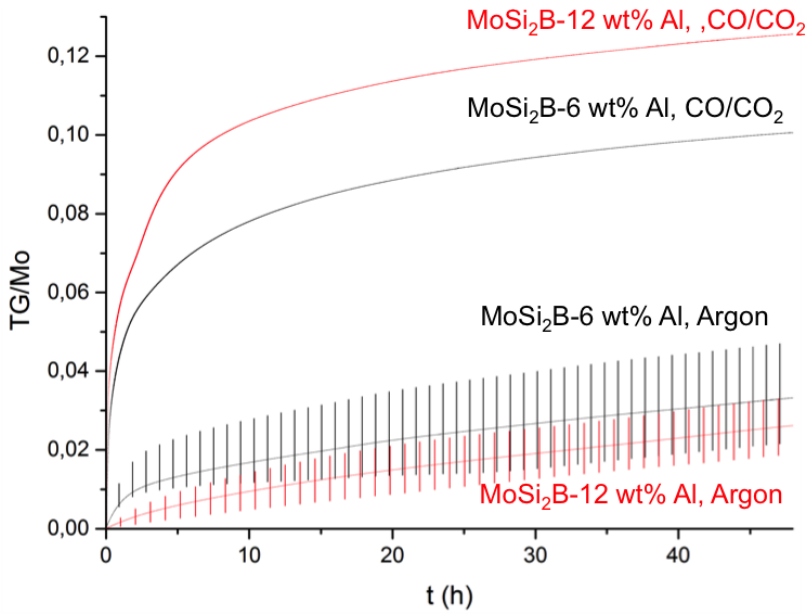

Figure 4.4: Mass gain curve $\Delta m/m_o$ as a function of annealing time (h) at 1100 °C for 48 hours for $MoSi_2B$-6 wt% Al and $MoSi_2B$-12 wt% Al powders in Argon and CO/CO_2 with ratio of 4.2.

During the annealing at T=200 °C (not shown), there was small mass loss (~0,1 mg) probably due to the evaporation of water vapour. From 200 °C to 1100 °C with 10 °C/min, there was only mass gain detected. No MoO_3 or other volatilised species were present in the furnace when cleaning after oxidation. Same experiment using empty crucible showed maximum mass loss of 0.3 mg and thus the effect of crucible to the mass-gain of particles during oxidation is neglected.

α-Al_2O_3 is formed as the main oxide accompanied with small amount of aluminium borate ($Al_{4.5}BO_{7.33}$ or Al_5BO_9) and Mo_5Si_3 for both particles (see XRD results in **Figure 4.5** for

oxidation in Ar and **Figure 4.6** for oxidation in CO/CO_2). Some peaks of Mo-B phase, as well as all Al and Si also disappeared after oxidation. Other than the intensity, the difference between oxidation in Ar and in CO/CO_2 is also on the carbide formation. Based on Rietveld refinement (see **Table A.2.1** for the result), the carbides are comprised with average of 1.8 wt% Molybdenum carbide (ζ-Mo_2C) and 2.6 wt% Molybdenum silicide carbide ($Mo_{4.8}Si_3C_{0.6}$).

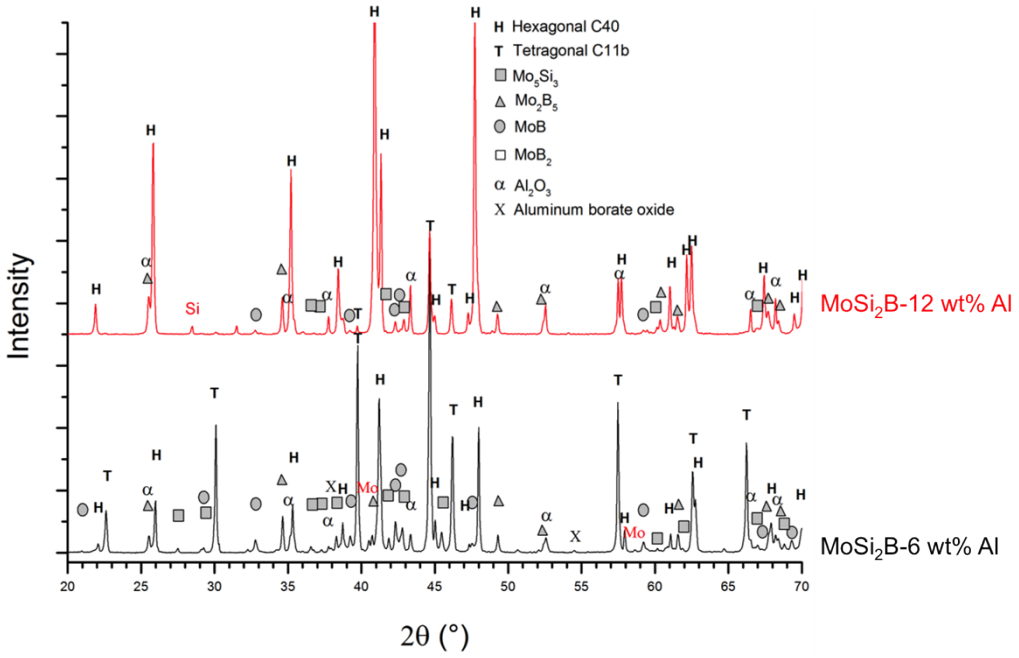

Figure 4.5: XRD for $MoSi_2B$-6 wt% Al and $MoSi_2B$-12 wt% Al powders after annealed for 48 hours at 1100 °C in Argon atmosphere.

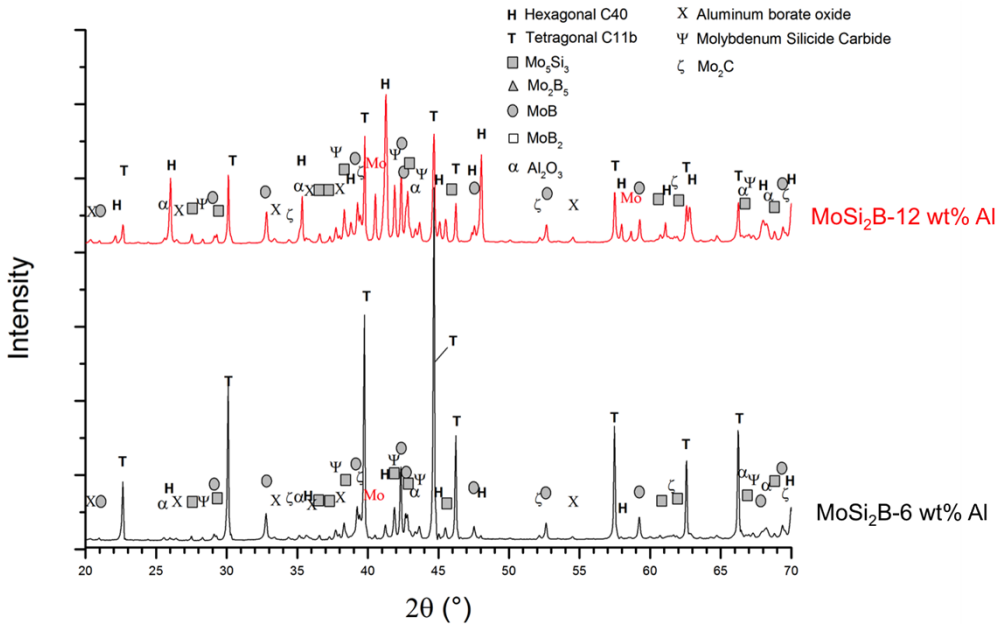

Figure 4.6: XRD for $MoSi_2B$-6 wt% Al and $MoSi_2B$-12 wt% Al powders after annealed for 48 hours at 1100 °C in CO/CO_2 (ratio of 4.2).

Table 4.4: Semi-quantitative analysis of weight fraction of $MoSi_2$ tetragonal $C11_b$ and $Mo(Si_{1-x},Al_x)_2$ hexagonal C40 between starting and after oxidation $MoSi_2B$-6 wt% Al and $MoSi_2B$-12 wt% Al powders with Rietveld refinement. See **Table A.2.1** for more detailed information

Crystal Structure	Starting powders		Oxidation at 1100 ˚C for 48h in Ar		Oxidation at 1100 ˚C for 48h in CO/CO_2	
	$MoSi_2B$-6 wt% Al	**$MoSi_2B$-12 wt% Al**	**$MoSi_2B$-6 wt% Al**	**$MoSi_2B$-12 wt% Al**	**$MoSi_2B$-6 wt% Al**	**$MoSi_2B$-12 wt% Al**
Tetragonal $C11_b$	18.9 wt%	3.0 wt%	48.0 wt%	0.8 wt%	62.3 wt%	22.1 wt%
Hexagonal C40	68.2 wt%	86.9 wt%	22.6 wt%	85.7 wt%	0.7 wt%	36.1 wt%

Table 4.5: Summary of chemical composition analysed with SEM/EDS of the oxide formed after oxidising at 1100 ˚C for 48 hours in Ar and CO/CO_2 with TGA for $MoSi_2B$-6 wt% Al and $MoSi_2B$-12 wt% Al powders

Oxidation atmosphere	Powders	Oxide shell	
		Morphology	**Composition**
Dry Argon	$MoSi_2B$-6 wt% Al	Whisker/bumps	SiO_2(+Al), and Al_2O_3(+Si), B_2O_3, $Al_{4.5}BO_{7.33}/AlBO_9$
		Columnar oxide	Al_2O_3
	$MoSi_2B$-12 wt% Al	Columnar oxide	Al_2O_3
		Whisker	Al_2O_3(+Si), B_2O_3, $Al_{4.5}BO_{7.33}/AlBO_9$
CO/CO_2 (4.2)	$MoSi_2B$-6 wt% Al	Whisker/bumps	Al_2O_3(+Si), $Al_{4.5}BO_{7.33}/AlBO_9$
		Film	SiO_2(+Al)
	$MoSi_2B$-12 wt% Al	Whisker/bumps	Al_2O_3(+Si), $Al_{4.5}BO_{7.33}/AlBO_9$

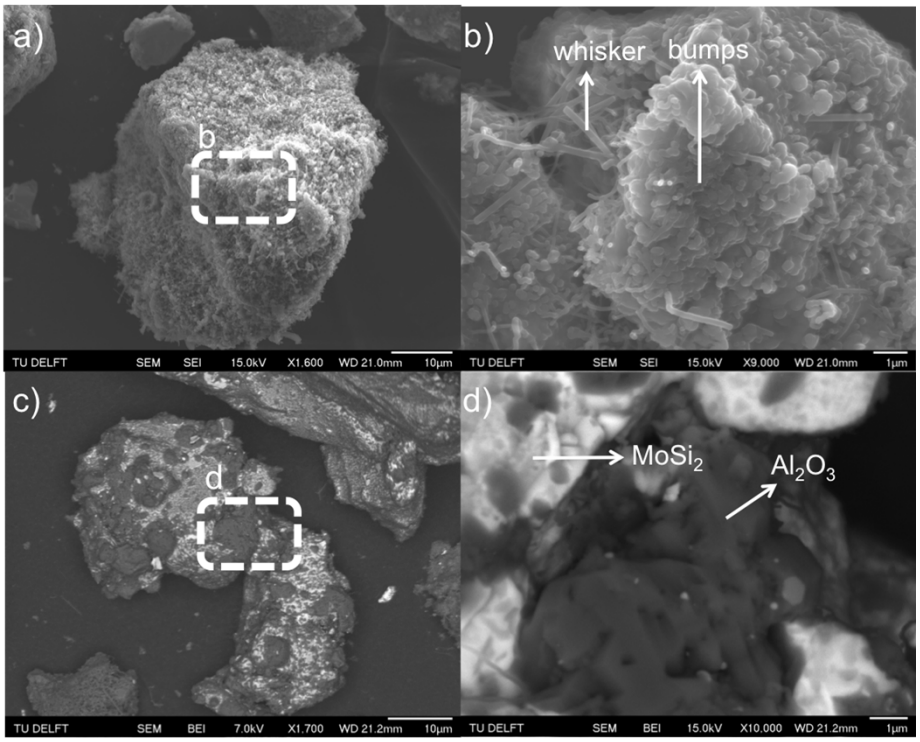

Figure 4.7: Oxide scale of $MoSi_2B$-6 wt% Al after oxidation treatment for 48 hours at 1100 ˚C in Ar.

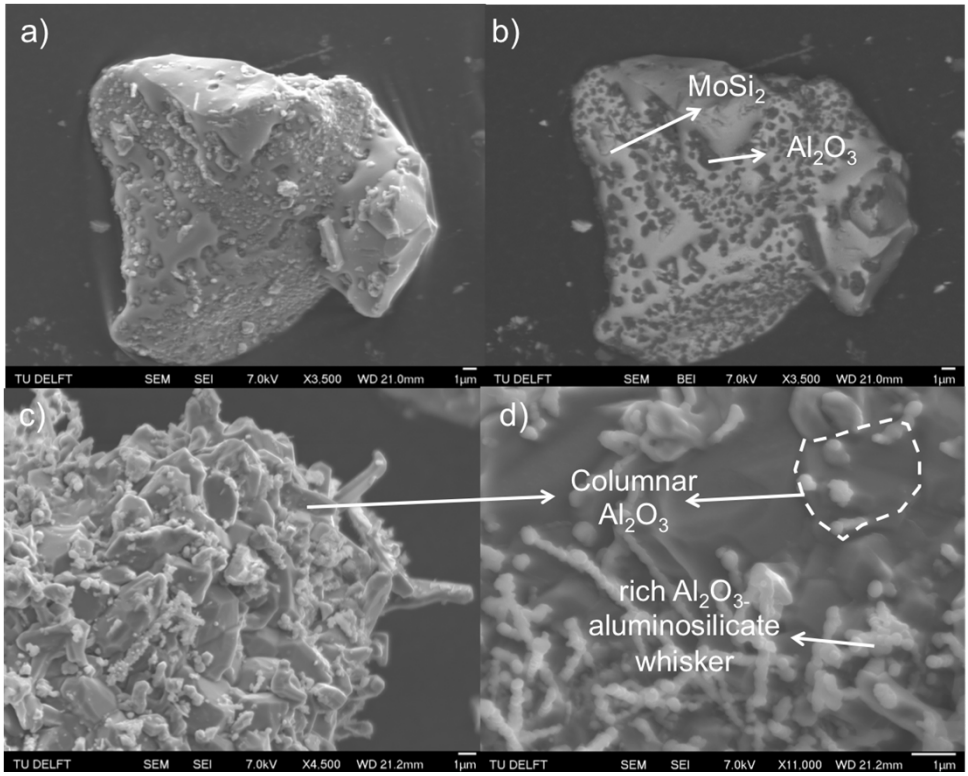

Figure 4.8: Oxide scale of $MoSi_2B$-12 wt% Al particles after oxidation treatment for 48 hours at 1100 °C in Ar.

Semi-quantitative analysis using Rietveld refinement between tetragonal $C11_b$ and hexagonal C40 was also done and it is shown in **Table 4.4**. The amount of hexagonal C40 phase in $MoSi_2B$-12 wt% Al particles after the oxidation in Argon is not significantly reduced and almost no new tetragonal $C11_b$ phase is formed. On the other hand, the peak of tetragonal $C11_b$ in $MoSi_2B$-6 wt% Al after oxidation is higher. On the contrary, oxidation in CO/CO_2 resulted in higher tetragonal $C11_b$ fraction in both powders.

The morphology and chemical composition of $MoSi_2B$-6 wt% Al and $MoSi_2B$-12 wt% Al particles after oxidation at 1100 °C is summarised in **Table 4.5**. The oxide of $MoSi_2B$-6 wt% Al particles analysed with SEM after oxidation in pure Argon can be seen in **Figure 4.7**. The oxide constituent after oxidation consists mainly of Al_2O_3, SiO_2 and mixture of Al_2O_3-SiO_2 oxide as shown in **Figure 4.7**(a-b). Partially oxidised $MoSi_2B$ particles are also found; see **Figure 4.7**(c-d) where BEI image clearly shows the contrast of oxide and Al-alloyed $MoSi_2B$ particle. Mixed Al_2O_3-SiO_2 oxide can consist of rich SiO_2 with a few incorporated Al and rich Al_2O_3 with a few incorporated Si. Both of these oxides inherit whiskers or bumps morphology. On the contrary, there are mainly scale of alumina and no rich SiO_2 found in the case of oxidation of $MoSi_2B$-12 wt% Al in pure Argon (see **Figure 4.8**). In **Figure 4.8**(c-d), the morphology of columnar alumina can be clearly seen. The whiskers are rich in Al_2O_3 with few Si incorporated in the compound. This compound inherits the morphology of

bumps/whisker similar with the case in $MoSi_2B$-6 wt% Al particles. Oxide of Aluminium borate cannot be detected due to the inaccuracy in detecting B element with EDS.

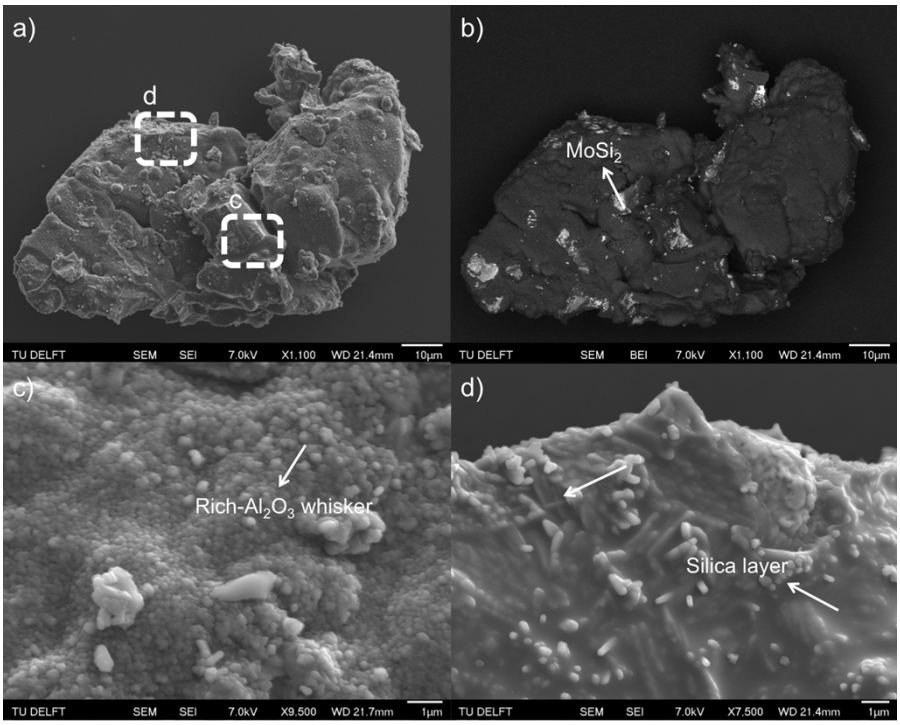

Figure 4.9: Oxide scale of $MoSi_2B$-6 wt% Al after oxidation treatment for 48 hours at 1100 ˚C in CO/CO_2.

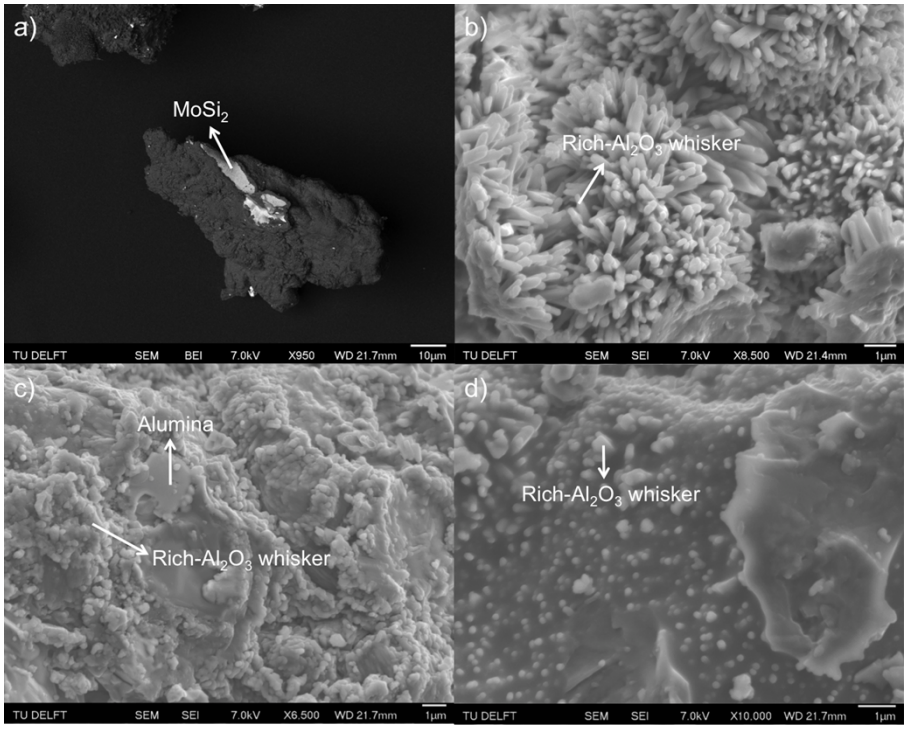

Figure 4.10: Oxide scale of $MoSi_2B$-12 wt% Al after oxidation treatment for 48 hours at 1100 ˚C in CO/CO_2.

According to **Figure 4.9**, oxidation of $MoSi_2B$-6 wt% Al and $MoSi_2B$-12 wt% Al in CO/CO_2 forms mainly of Al_2O_3 with a few incorporated Si. In the case of $MoSi_2B$-6 wt% Al, the main oxide is rich Al_2O_3 with a few incorporated Si inheriting the morphology of bumps and short-whiskers as seen in **Figure 4.9**(c-d). Rich-SiO_2 film instead of whisker is also formed (**Figure 4.9**(d)). In the case of $MoSi_2B$-12 wt% Al oxidation in CO/CO_2, oxide rich in Al_2O_3 with a few incorporated Si is the only oxide forming (see **Figure 4.10**(b-d)). No columnar alumina is formed anymore as in the case oxidation of $MoSi_2B$-12 wt% Al in Argon.

4.2 $MoSi_2$ in situ encapsulation

4.2.1 Sintering of YSZ + Al-alloyed $MoSi_2B$ composite via spark plasma sintering (SPS)

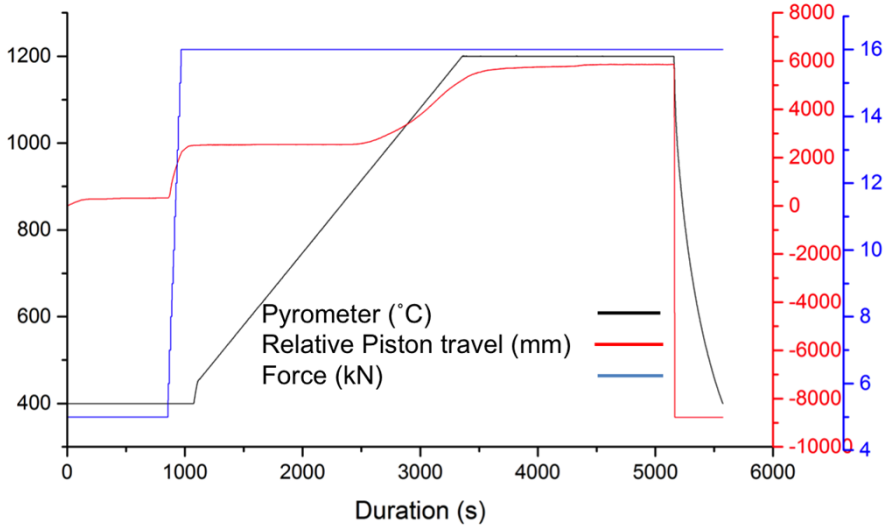

Figure 4.11: Piston displacement curve in SPS during the sintering of YSZ+10MSBA composite.

After mixing YSZ and Al-alloyed $MoSi_2B$ powders (cf. **Section 3.2.1**), composites were made with Spark Plasma Sintering (SPS). There were three YSZ+10MSBA composites prepared: YSZ+10MSB2A, YSZ+10MSB6A and YSZ+10MSB12A (see **Table 3.1**). The colour of the composite was dark-grey after sintering process even though the dominant of the mixture was 90 vol% white 3YSZ Tosoh powders. From the piston displacement curve in SPS of all composites (**Figure 4.11**), it is shown that the sintering/densification is started around ~T=1000 ˚C due to the piston movement towards the sample. The microstructure of cross-section of YSZ+10MSBA composites was investigated with SEM and can be seen in **Figure 4.12**). It is observed that the composite shows a dense material and no YSZ grains are seen.

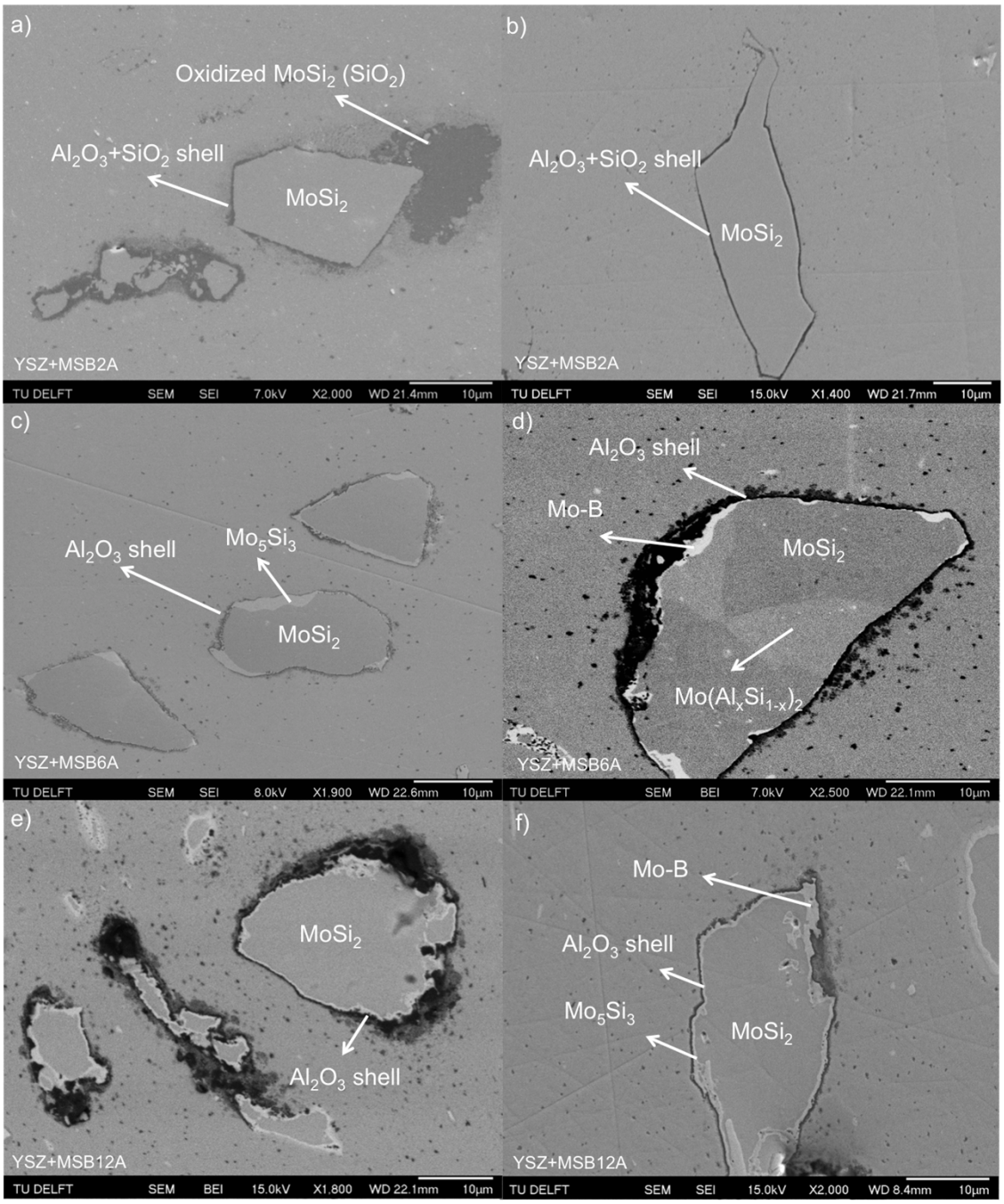

Figure 4.12: Cross-section microscopic view of YSZ + Al-alloyed $MoSi_2B$ (YSZ+10MSBA) composite after sintering with SPS by Scanning Electron Microscope (SEM) for particles in YSZ+10MSB2A composite ((a) and (b)), in YSZ+10MSB6A composite ((c) and (d)), and in YSZ+10MSB12A composite in ((e) and (f)).

In order to obtain the variation of the composition of the particle in the composites, 20-50 particles were analysed using SEM/EDX (see **Figure 4.12** for the cross-section microscopic view) and EPMA (see **Table 4.6** for the result). It is found that the particles are mainly composed of $Mo(Al_x,Si_{1-x})_2$, $MoSi_2$, Mo_5Si_3, SiO_2 (oxidized $MoSi_2$) and Mo-B phase. $Mo(Al_x,Si_{1-x})_2$ is usually present with lighter grey region compared to the darker grey $MoSi_2$

(see **Figure 4.12**(c)) which having a maximum of ~1.2 wt% Al. From the EPMA, $MoSi_2B$-6 wt% Al has an average of $1.3^{+2.1}_{-1.1}$ wt% Al and $MoSi_2B$-12 wt% Al an average of $1.9^{+7.9}_{-1.8}$ wt% Al. Underneath the alumina shell, Mo_5Si_3 is formed. The average thickness of Mo_5Si_3 is also different for the three composites. Very thin and rarely Mo_5Si_3 is formed in YSZ+10MSB2A composite, whereas thicker Mo_5Si_3 was formed in YSZ+10MSB6A and YSZ+10MSB12A, respectively. The particles are surrounded with oxide shell. The particles in YSZ+10MSB6A (**Figure 4.12**(c-d)) and YSZ+10MSB12A (**Figure 4.12**(e-f)) are encapsulated with alumina shell. However not all particles in YSZ+$MoSi_2B$-2 wt% Al (**Figure 4.12**(a-b)) are encapsulated. In this case, the shell is composed of thin SiO_2 and Al_2O_3+SiO_2. Slightly more particles are also heavily or fully oxidised to silica in the YSZ+10MSB2A composite. It is also important to note also that the shell around particles is not homogeneous.

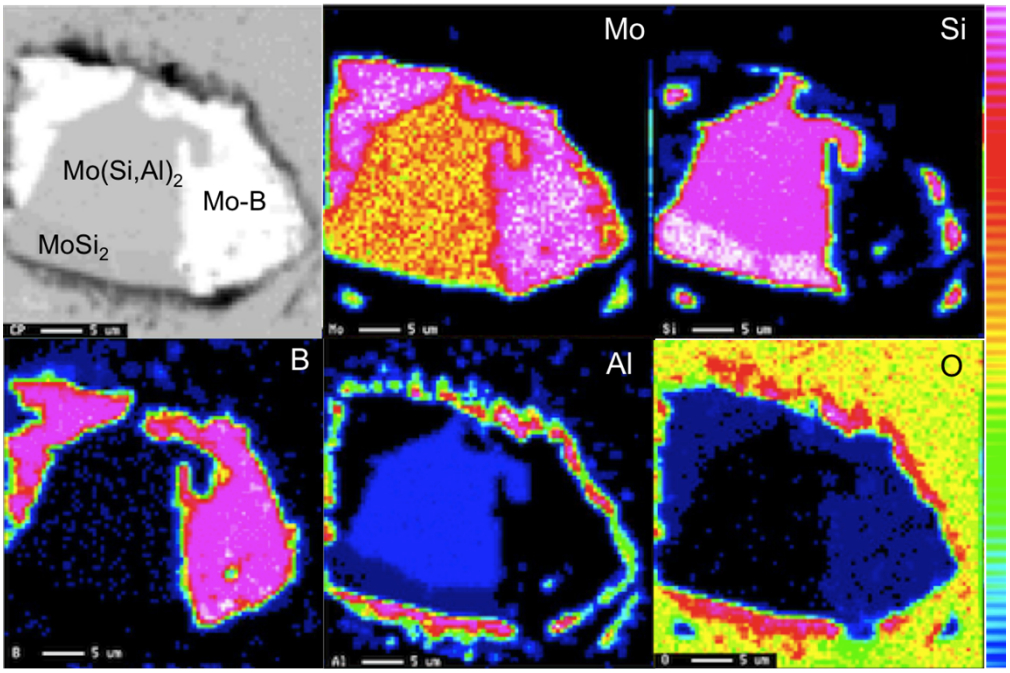

Figure 4.13: EPMA Elemental mapping of a Al-alloyed $MoSi_2B$ particles for Mo, Si, B, Al and O element in YSZ + Al-Alloyed $MoSi_2B$-6 wt% Al (YSZ+10MSB6A) composite after sintering process.

Element mapping with EPMA is shown in **Figure 4.13**. In the Mo-B region, it is shown the complex composition with the presence of Mo, B and Si. MoB, MoB_2 and Mo_2B_5 indeed were detected however often accompanied with varying Si and O as well. However, from the mapping it can be proven that the low amount of Si and O are found in Mo-B region.

4.2.2 Aluminium depletion in low pO_2 annealing

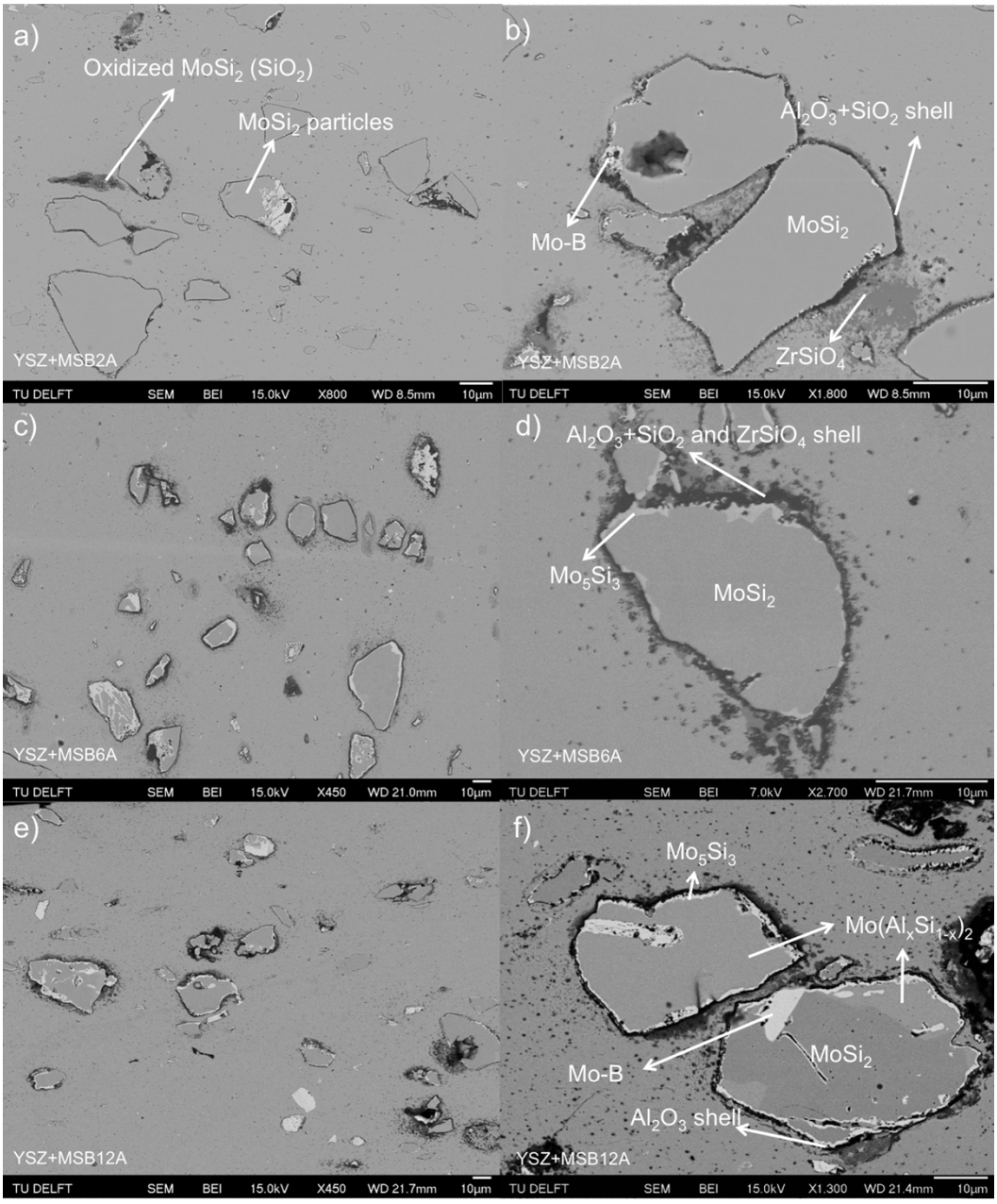

Figure 4.14: Cross-section microscopic view of YSZ + Al-alloyed $MoSi_2B$ (YSZ+10MSBA) composite after low pO_2 annealing in pure Argon with Scanning Electron Microscope (SEM). The particles (a) and (b) in YSZ+10MSB2A composite, (c) and (d) in YSZ+10MSB6A composite, (e) and (f) YSZ+10MSB12A composite.

In order to thicken the alumina shell, all YSZ+10MSBA composites were annealed at 1100 °C for 16 hours in low pO_2 atmosphere. Two different atmospheres were used: pure Argon and CO/CO_2 with ratio of 4.2; cf. **Section 3.2.2**. Statistical analysis of the Al content in the $MoSi_2B$ particles as well as shell composition and thickness was also done and the results are presented in **Table 4.6**. Overall, a thicker shell is formed for all composites after low pO_2 annealing, even though the shell constituent is different (see **Figure 4.14**). Zircon ($ZrSiO_4$), SiO_2, and mixture of SiO_2+Al_2O_3 shell are formed around the particles in

YSZ+10MSB2A composite (**Figure 4.14**(a-b)) and YSZ+10MSB6A composite (**Figure 4.14**(c-d)). On the contrary, zircon and silica are not formed around the particles in the case of YSZ+10MSB12A composite in **Figure 4.14**(e-f). The comparison of shell composition and thickness after SPS and low pO_2 annealing process in pure Argon is shown in **Figure 4.15**. EDX linescan in one of the shell around $MoSi_2B$-6 wt% Al particles shows the presence of SiO_2 with few Al_2O_3 (Al_2O_3+SiO_2 shell) underneath Al_2O_3 and $ZrSiO_4$ shell (**Figure 4.15**(g)). On the contrary, the shell of particles in YSZ+10MSB12A composite consists only of alumina.

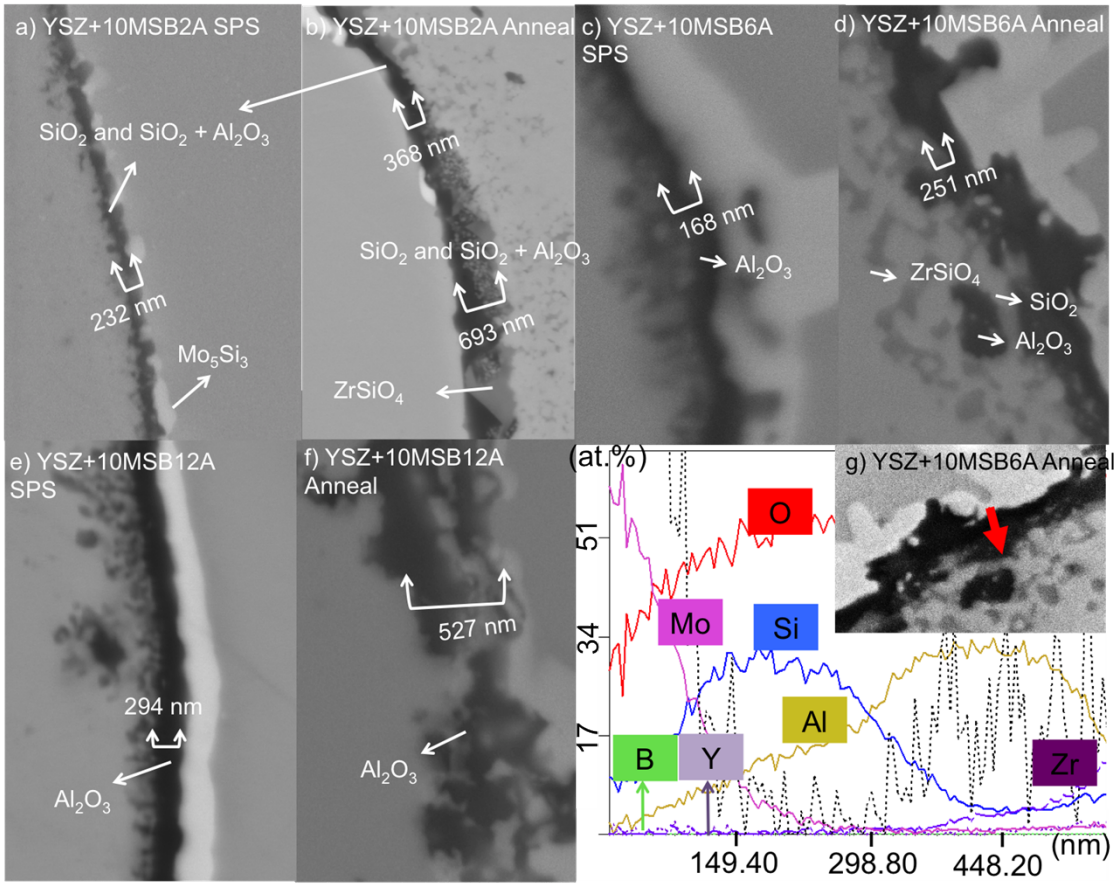

Figure 4.15: Shell composition and the thickness evolution for YSZ + Al-Alloyed $MoSi_2B$ (YSZ+10MSBA) composite after (a), (c), (e) SPS and (b), (d), (f) low pO_2 annealing in pure Argon. (g) shows the linescan of shell around particle in YSZ+ $MoSi_2B$-6 wt% Al (YSZ+10MSB6A) composite

According to the SEM/EDS analysis in **Figure 4.14**, the phases present inside and around the particles of all composites after low pO_2 annealing are the same after sintering in SPS: $Mo(Al_x,Si_{1-x})_2$, $MoSi_2$, Mo_5Si_3, and Mo-B. Al is mainly depleted from the particles for all composites. However, in the case of YSZ+10MSB6A and YSZ+10MSB12A composite, few particles still contain lighter-grey $Mo(Al_x,Si_{1-x})_2$. The continuous Mo_5Si_3 underneath the shell of the particles are also thicker in YSZ+10MSB6A and YSZ+10MSB12A composite. Faint Mo_5Si_3 starts to form as well for particles in YSZ+10MSB2A composite. Most particles in all

composite are mainly still protected from oxidation, only a few are heavily/fully oxidised to silica and more can be found in the case of particles in YSZ+10MSB2A composite.

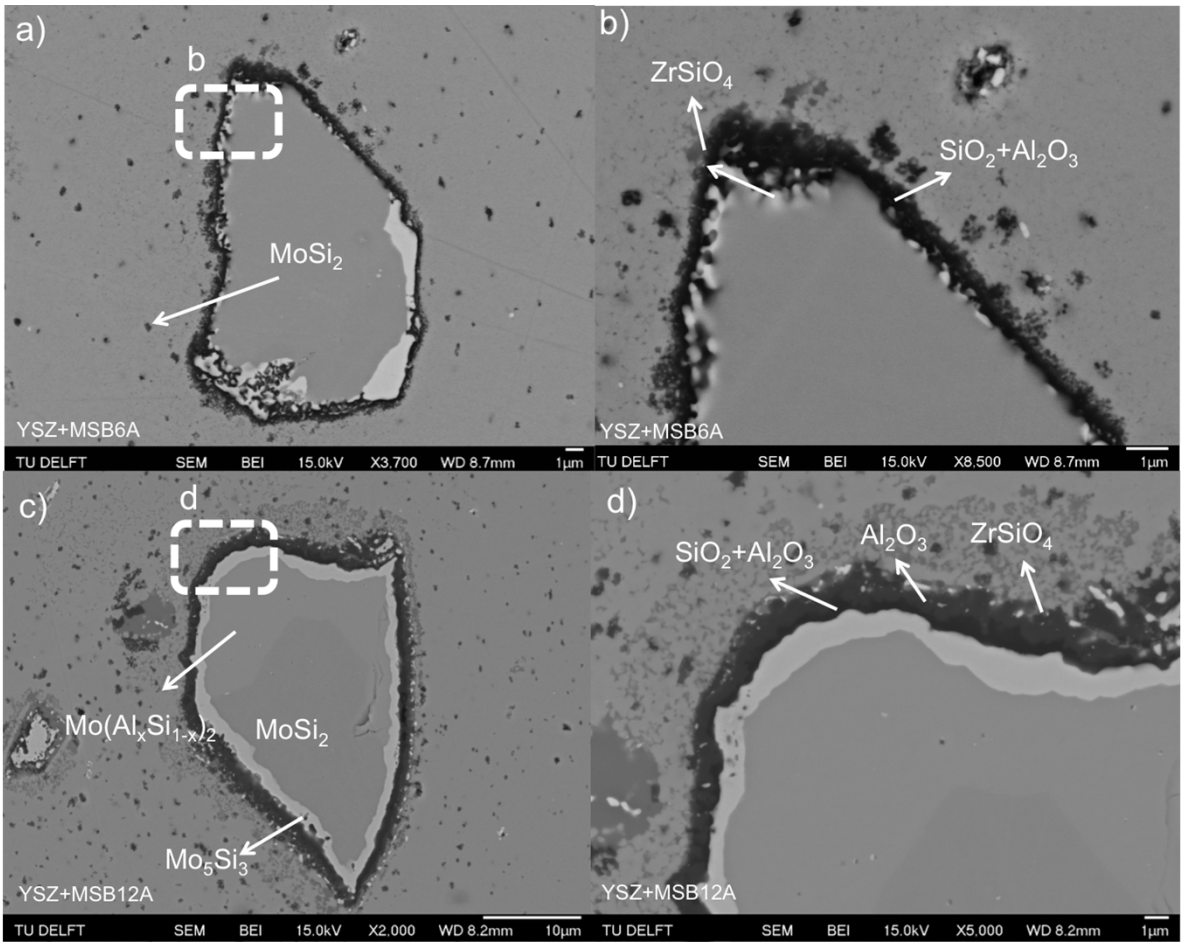

Figure 4.16: Particles in YSZ + $MoSi_2B$-6 and 12 wt% Al (YSZ+10MSB6A and YSZ+10MSB12A) composite after annealing in CO/CO_2 for 16 hours. (a) and (c) show the BEI image of one particle, (b) and (d) show the magnification of the shell.

Low pO_2 annealing in CO/CO_2 (with ratio of 4.2) atmosphere was also conducted for YSZ+10MSB6A and YSZ+10MSB12A composite. SEM images can be seen in **Figure 4.16**. No particular difference between YSZ+10MSB6A composite annealed in pure Argon and CO/CO_2. In both cases zircon was found as a sign of silica presence in the shell around the particles. However, annealing in low pO_2 in CO/CO_2 for YSZ+10MSB12A composite formed silica and zircon in the shell as well, unlike in the case of oxidation in pure Argon.

4.2.3 Microcapsule stability test

After the encapsulation of $MoSi_2B$ particles, the sample was exposed directly at 1100 °C in air for total of 100 hours to check the stability of the encapsulated particle. After the exposure, the samples turned their colour to light and eventually to ivory/yellow. Regardless,

all composites were still intact. Visually the composite shows two different colours of the composite: yellow region at the outer and dark-grey region at the inner side (**Figure 4.17**). Crack appears between those two regions. For all composites, cracks and pores are found and more particles are oxidised in the outer side.

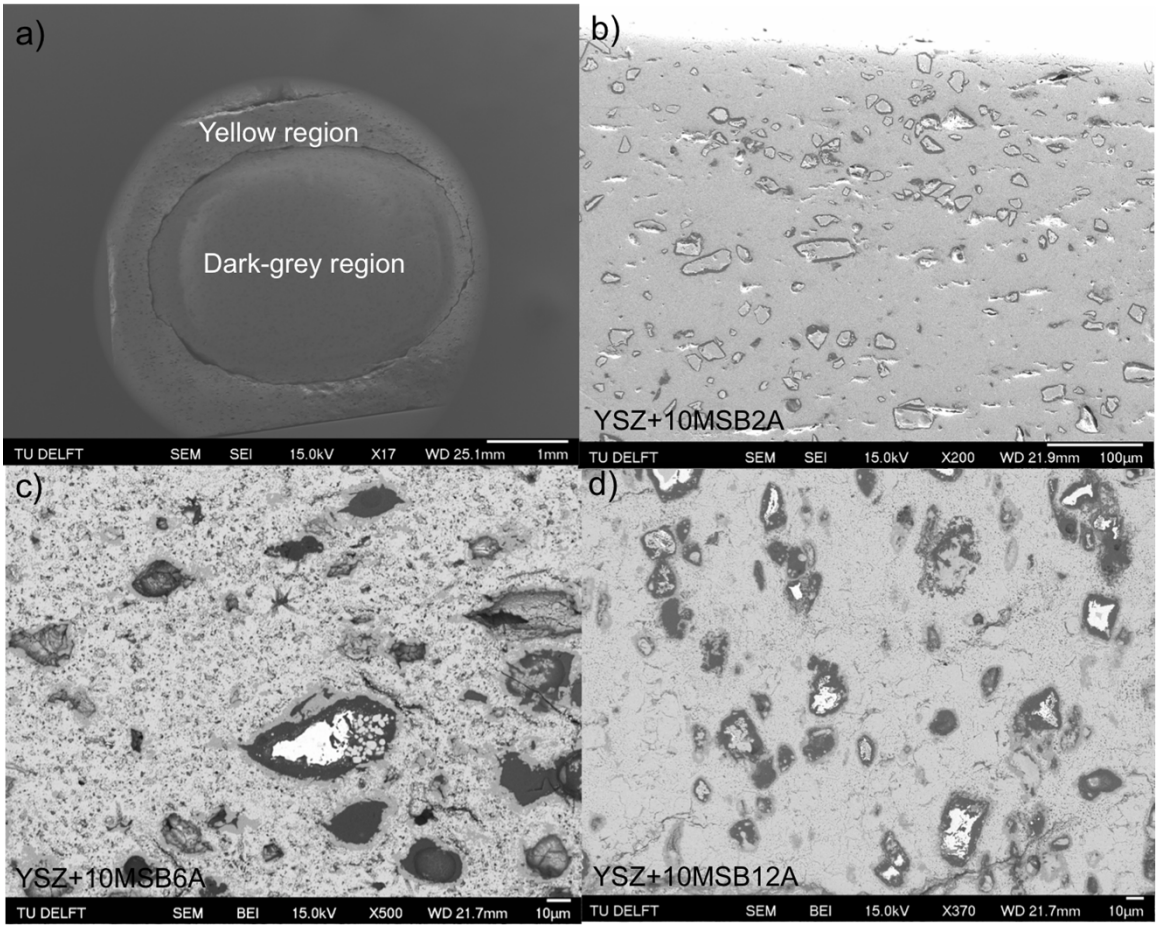

Figure 4.17: Cross-section microscopic view of YSZ + Al-alloyed $MoSi_2B$ (YSZ+10MSBA) composites after microcapsule stability test at 1100 °C in air for 100 hours. (a) shows the outer side (yellow region) and inner side (dark-grey region). The particles are shown in (b) for YSZ+10MSB2A, (c) for YSZ+10MSB6A, (d) for YSZ+10MSB12A composite

For the particles in the inner side, the shell of the particles is comprised of Al_2O_3, SiO_2, mixed Al_2O_3 and SiO_2, and $ZrSiO_4$ in the case of all composites. The SEM images for the particles in all of the composites are shown in **Figure 4.18**. Shell becomes thicker with previously formed alumina or with newly formed silica and zircon. More alumina is now found with mixed silica. Shell composition for a particle in YSZ+10MSB12A was analysed with EDS linescan and it is shown in **Figure 4.18**(e). The shell composition from inside the particle towards the matrix is mixed SiO_2-Al_2O_3, Al_2O_3 and $ZrSiO_4$ oxide. Mo_5Si_3 underneath the shell for all composites are now also thicker.

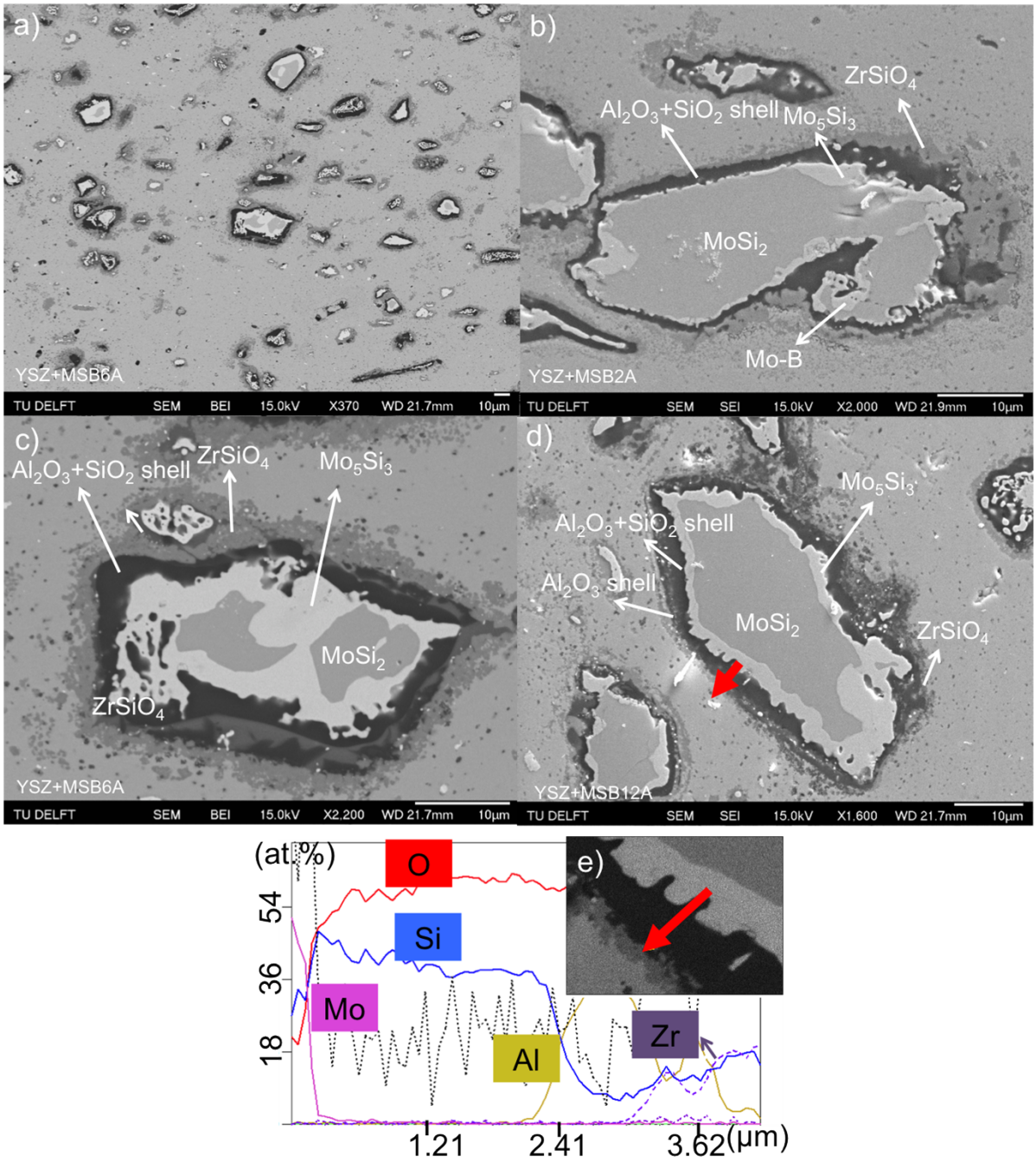

Figure 4.18: Cross-section microscopic view of YSZ + Al-alloyed $MoSi_2B$ (YSZ+10MSBA) composites after microcapsule stability test at 1100 °C in air for 100 hours. (a) shows the low magnification showing the trend of particles in YSZ+10MSB6A composite. (b) shows the particles in YSZ+10MSB2A composite, (c) in YSZ+10MSB6A composite, (d) in YSZ+10MSB12A composite. (e) (See arrow in (d)) linescan of the shell.

Table 4.6: Statistical data on YSZ + Al-alloyed $MoSi_2B$ (YSZ+10MSBA) composites s after SPS, low pO_2 annealing and microcapsule stability test. Al content was analysed from 50 particles using EPMA.

Sample	Shell composition				Fully oxidized particles	*†Remaining Al (wt%)	Shell thickness (µm)
	Al_2O_3	SiO_2	Al_2O_3+SiO_2	$ZrSiO_4$			
After Spark Plasma Sintering (SPS)							
YSZ+10MSB2A		✓	🡅		1%	0.10	$0.25^{+0.71}_{-0.19}$
YSZ+10MSB6A	🡅				0.5%	$1.3^{+2.1}_{-1.1}$	$0.24^{+0.29}_{-0.19}$
YSZ+10MSB12A	🡅				0.5%	$1.9^{+7.9}_{-1.8}$	$0.53^{+0.99}_{-0.34}$
After low pO_2 annealing in pure Argon							
YSZ+10MSB2A		✓	🡅	✓	2%	0	$0.29^{+1.49}_{-0.97}$
YSZ+10MSB6A	🡅	✓	🡅	✓	2%	$0.1^{+2.4}_{-0.1}$	$0.67^{+0.87}_{-0.43}$
YSZ+10MSB12A	🡅				1%	$1.0^{+6.1}_{-1.0}$	$0.48^{+1.02}_{-0.30}$
After low pO_2 annealing in CO/CO_2 of 4.2							
YSZ+10MSB6A	🡅	✓	🡅	✓		-	$0.60^{+0.85}_{-0.44}$
YSZ+10MSB12A	🡅	✓	🡅	✓		-	$1.10^{+1.01}_{-0.72}$
After Microcapsule Stability Test							
YSZ+10MSB2A	✓	✓	🡅	✓	2.5%	0	$1.99^{+0.66}_{-0.74}$
YSZ+10MSB6A	✓	✓	🡅	✓	2%	0	$5.40^{+3.77}_{-2.66}$
YSZ+10MSB12A	✓	✓	🡅	✓	1.5%	0	$2.20^{+1.63}_{-0.80}$

*Taken out from 50 particles with SEM/EDX and EPMA
†With EPMA and Including $Mo(Al_x,Si_{1-x})_2$ → $MoSi_2$

✓□□□□□Present
🡅 Majority

4.3 Crack-gap filling

The width of the crack-gap after the indentation with Vickers Indenter of 200-300 N was in the range of 0.1-1 µm for both YSZ+10MSB6A composite with pre-encapsulated and in situ encapsulated particles. **Figure 4.19**(a) shows an example of the indentation with cracks going through the particles for pre-encapsulated YSZ+10MSB6A composite. **Figure 4.19**(c-d) shows the crack-gap before and after filled crack with oxide. **Figure 4.19**(e-f) shows also the filled crack however unfilled crack denoted with zirconia matrix underneath the crack is also observed. **Figure 4.20**(a) shows the crack going straight through the particles. However the cracks are more occasionally going through the interface of particle (i.e. $MoSi_2$ or Mo_5Si_3) and shell (i.e. Al_2O_3 or mixed Al_2O_3-SiO_2) as shown in **Figure 4.20**(b). After the healing treatment at 1100 °C, the crack-gap became smaller. Thus polishing was done to investigate oxidation product deeper into the crack gap. **Figure 4.20**(c-h) shows the surface condition with SEI/BEI images of YSZ+10MSB6A pre-encapsulated after the healing treatment (1, 4 and 16 hours) and after polishing. Zircon may form around the crack as seen in **Figure 4.20**(c-d). **Figure 4.20**(e-f) and **Figure 4.20**(g-h) show the filled crack-gap with oxide. Analysis with EDS for the filling shows signal up to 30 at% Si. However, most of the time the signal of Si is very low (1-5 at%) not corresponding with SiO_2 or $ZrSiO_4$

healing product. Overall, the successful rate of crack-gap filling is about 50% and the trend is similar regardless of the healing time.

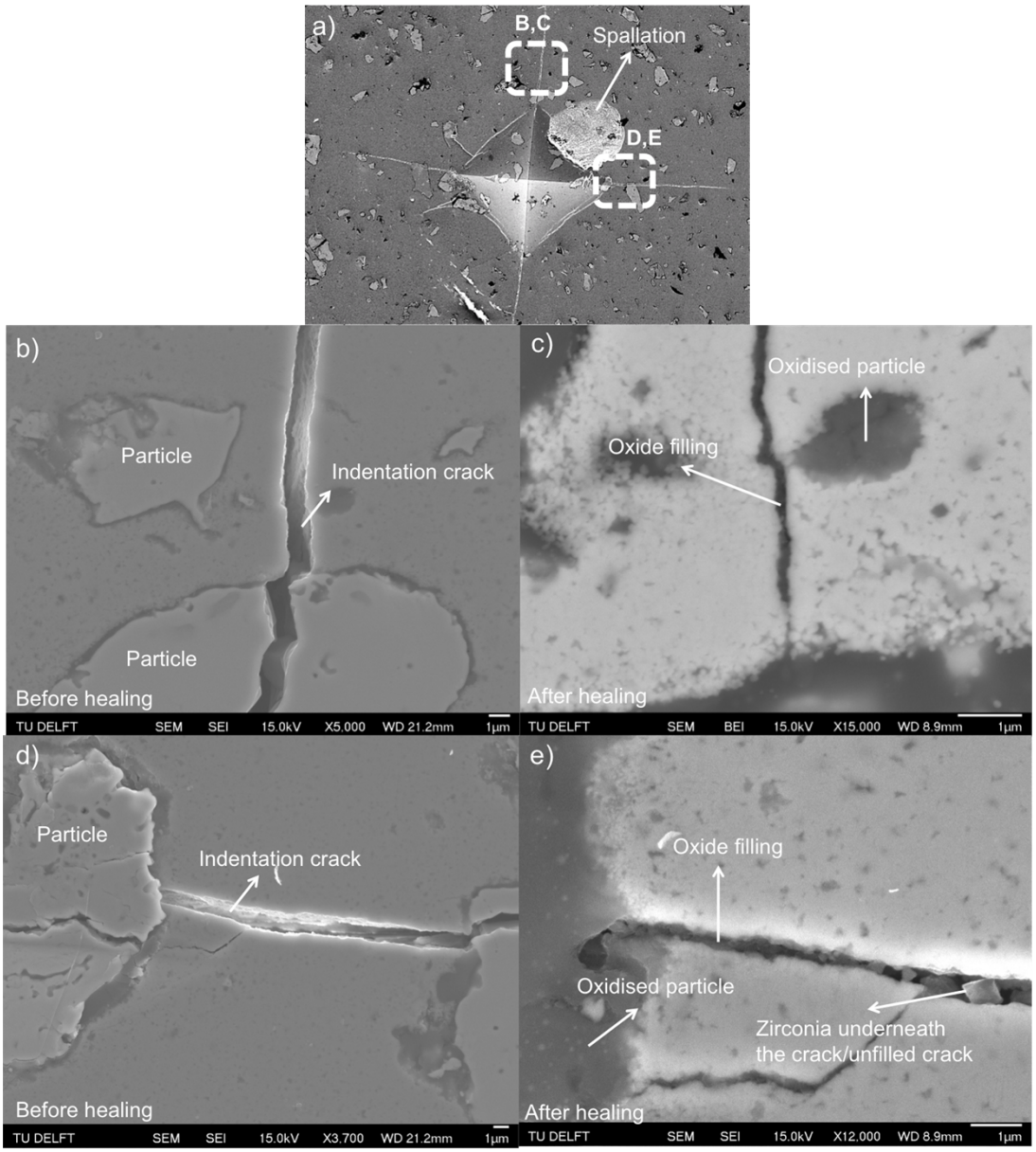

Figure 4.19: (a) Example of Vickers indentation and indentation crack YSZ + pre-encapsulated $MoSi_2B$-6 wt% Al (YSZ+10MSB6A) composite. (b) and (c) show the crack indentation before healing, (d) and (e) show the filled and partially filled crack by silica.

The composite of in situ encapsulated YSZ+10MSB6A composite was only healed for 4 hours at 1100 °C in air. **Figure 4.21** shows the SEI/BEI images of this sample after healing and polishing treatment. Similar to the case of pre-encapsulated YSZ+10MSB6A composite, there is oxide filling the crack-gap. According to **Figure 4.21**(a-d), it is found that the oxide filling is silica. Zircon is also observed in **Figure 4.21**(e-h) along the crack or at few sports along the crack-gap. However, with EDS observation it is only found up to 10 at% Si and

also sometimes with a very few Al. Same as before, cracks are filled with about 50% successful rate.

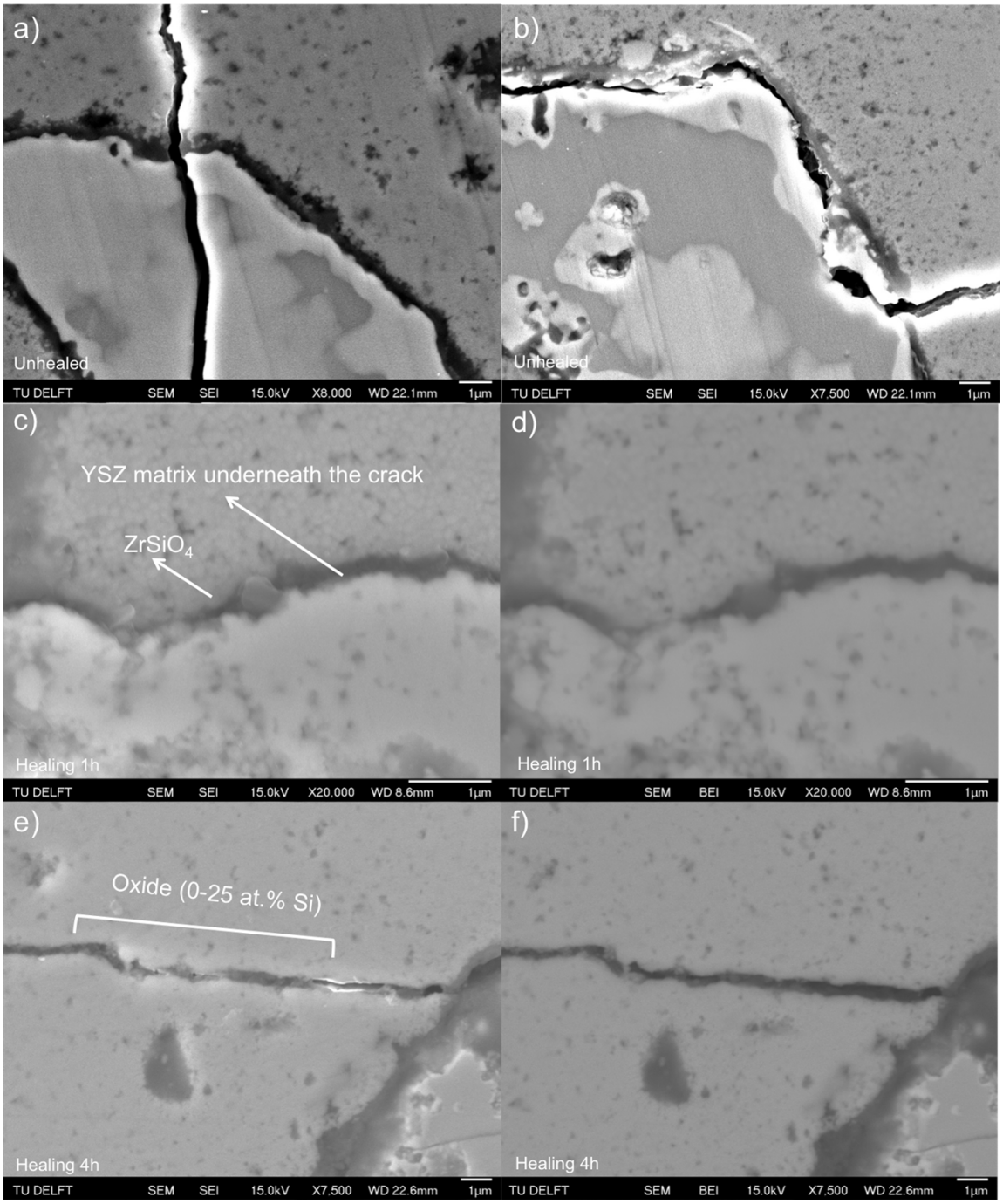

Figure 4.20: Surface observation YSZ + pre-encapsulated $MoSi_2B$-6 wt% Al (YSZ+10MSB6A) composite (a) and (b) after indentation. (c) and (d) show the condition after healing for 1 hour, (e) and (f) show the condition after healing for 4 hours, (g) and (h) show the condition after healing for 16 hours (images of healing was taken after polished). (c),(e),(g) show the SEI images and (d),(f),(g) show the BEI images.

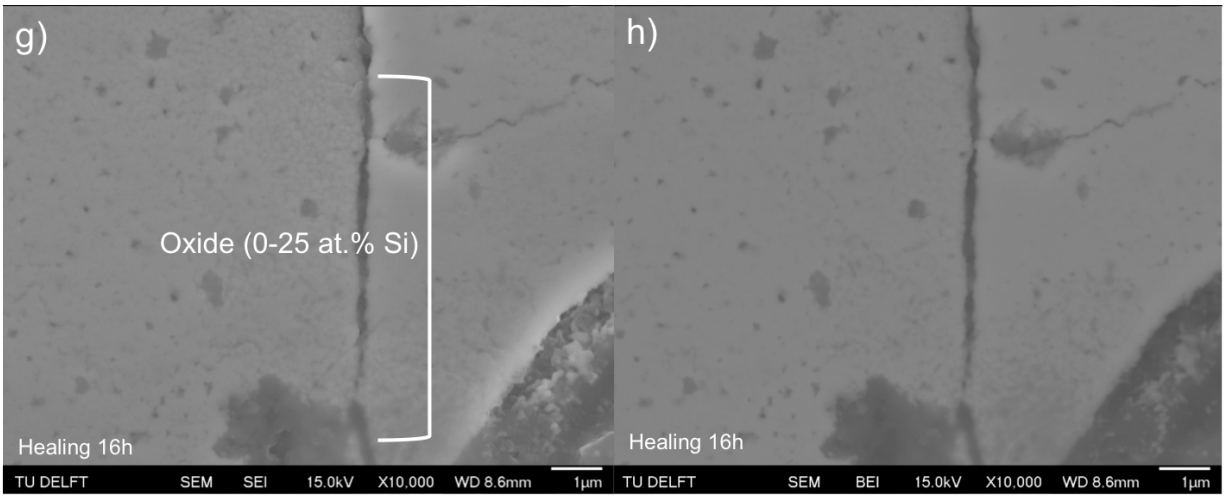

Figure 4.20: *(continued).*

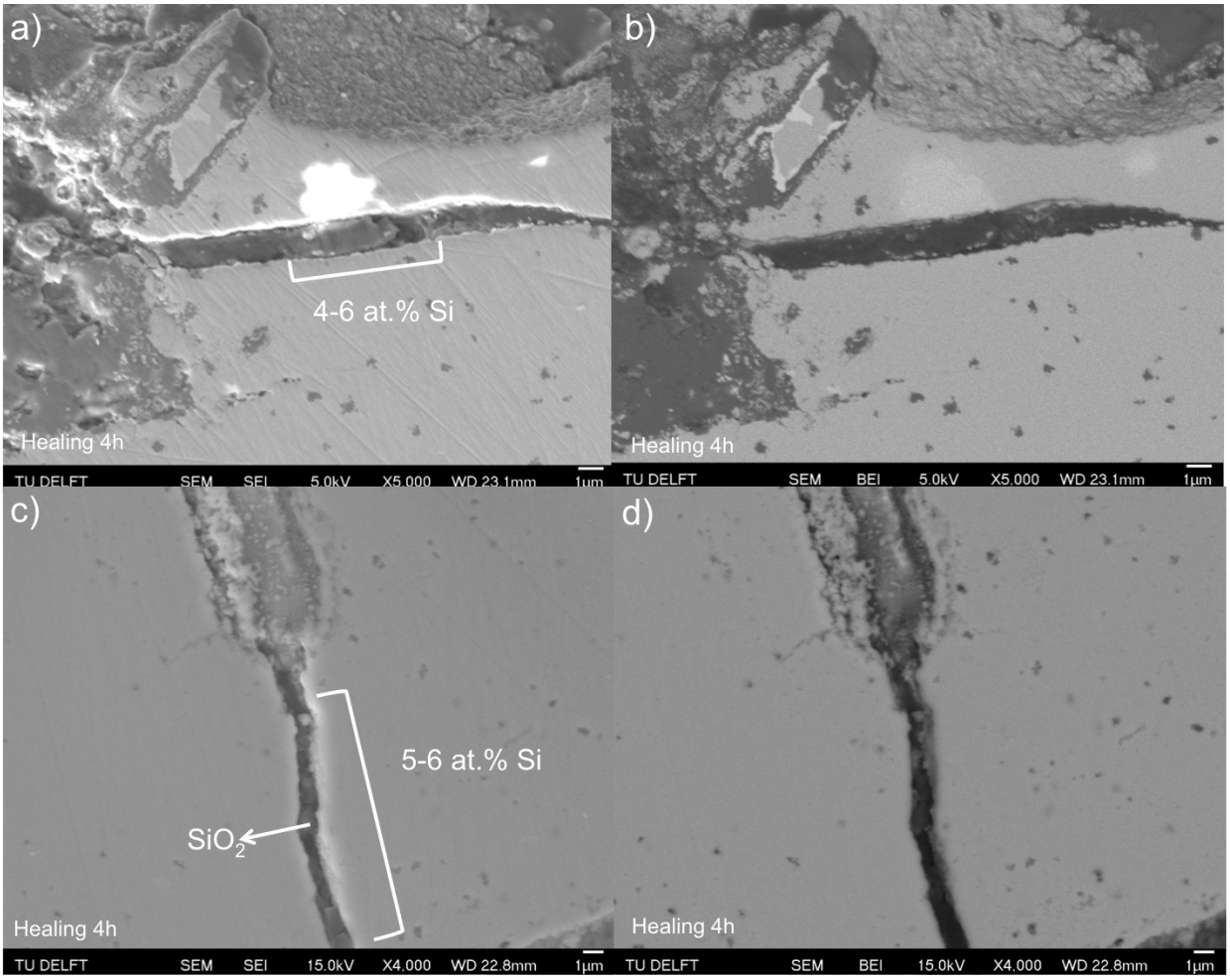

Figure 4.21: Surface observation of different cracks of YSZ + in situ encapsulated $MoSi_2B$-6 wt% Al (YSZ+10MSB6A) composite healed at 1100 °C in air for 4 hours. (a),(c),(e),(g) show the SEI images. (b),(d),(f),(h) show the BEI images.

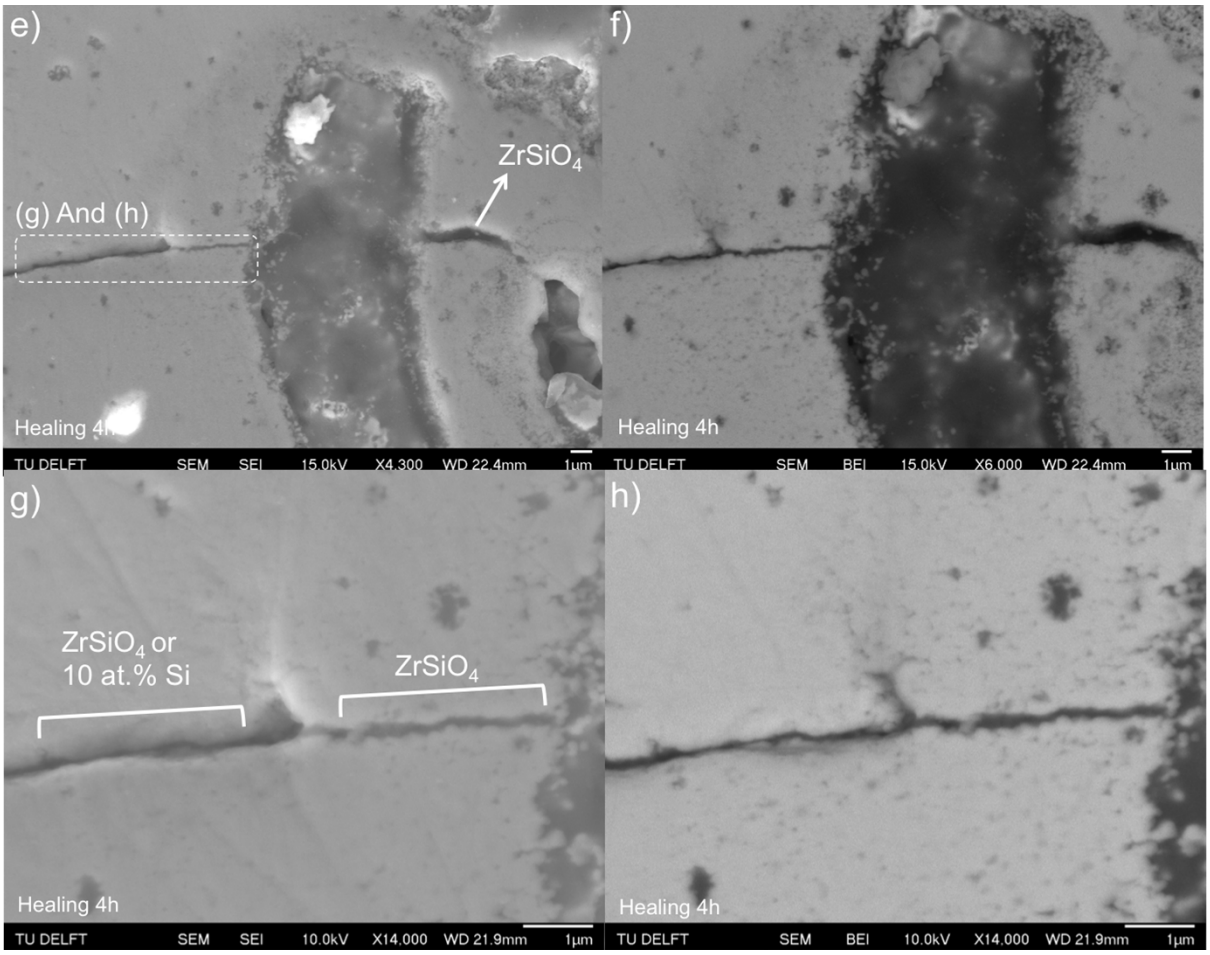

Figure 4.21: *(continued).*

5

Discussion

5.1 Powders

5.1.1 Oxide growth kinetics

The plot of normalised mass gain $\Delta m/m_o$ in function of isothermal annealing time *t* for $MoSi_2B$-6 wt% Al and $MoSi_2B$-12 wt% Al is shown in **Figure 4.4**. The complex surface area inherited by the irregular (e.g. **Figure 4.3**) and quite inhomogeneous size (e.g. **Figure 4.1**) of powders sample caused the different results between 3 experiments for each Al-alloyed $MoSi_2B$ (the 3 different results ware represented with vertical line along the mass-gain curve). The power law of oxidation is expressed as[59, 60]:

$$\Delta m = kt^n \tag{5.1}$$

Where Δm is the weight change, *k* is the oxidation rate constant and *n* is the growth rate exponent. With the derivation from **(5.1)** the growth rate exponent *n* can be calculated by,

$$n = \frac{\delta(\log(\Delta m))}{\delta(\log(t))} \tag{5.2}$$

To obtain the growth rate exponent *n*, Equation **(5.2)** can be rewritten as:

$$n = \frac{\partial(\Delta m)}{\partial(\mathrm{t})} \cdot \frac{\Delta m}{t} \tag{5.3}$$

With the equation above, the growth rate exponent *n* versus the isothermal annealing time *t* can be plotted as shown in **Figure 5.1**(a). Oxidation in pure Argon resulted in growth rate exponent *n* of 1.3-2.2 for $MoSi_2B$-6 wt% Al and 1.1-1.5 for $MoSi_2B$-12 wt% Al. Therefore, both powders showed parabolic-like rate law kinetics. This suggests that the oxygen anion or metal cation diffusion through oxide as the rate-limiting step[61]. Plotting the growth rate exponent *n* with the same equation for oxidation in CO/CO_2 resulted in inconstant *n* (**Figure**

5.1(a)) showing that it does not satisfy power law. However, the oxide growth in CO/CO_2 can be described with a logarithmic rate law as can be seen in **Figure 5.1**(b) showing the good fit of R^2. Logarithmic rate law denotes more protective shell against oxidation.

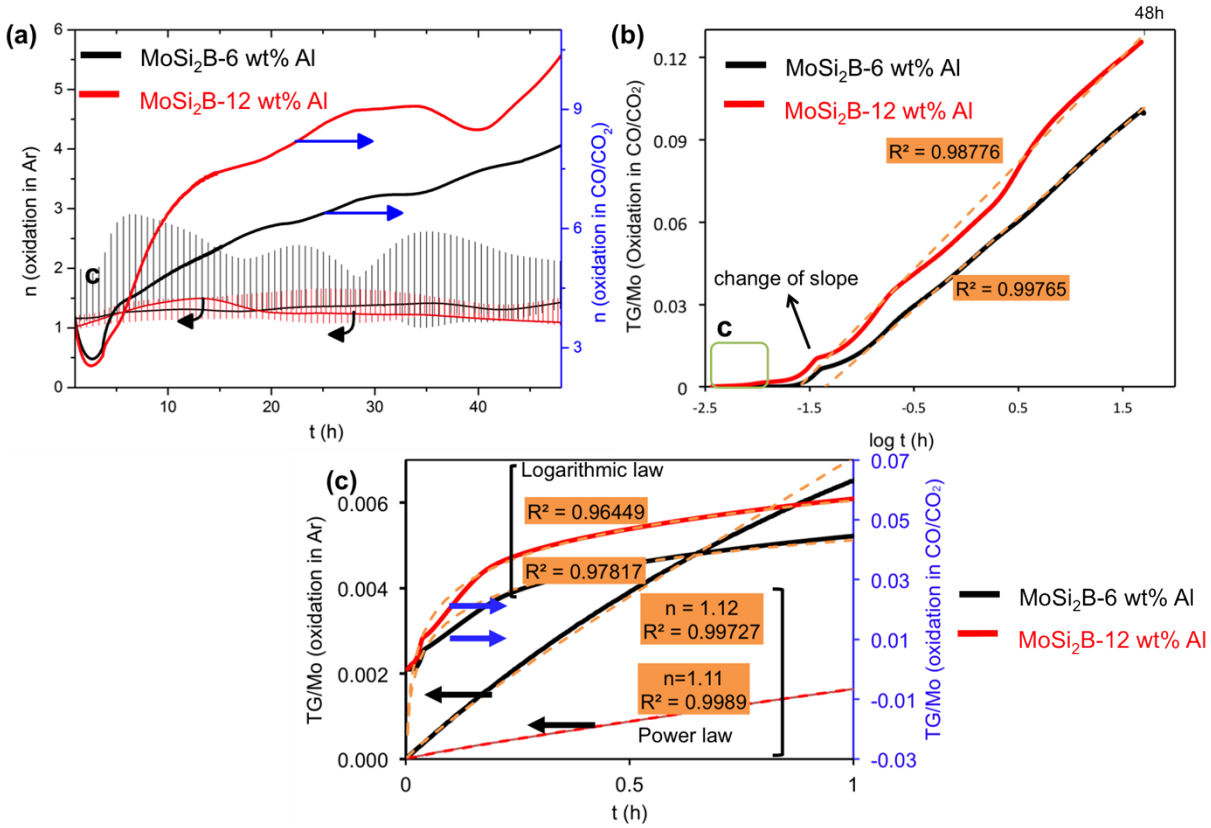

Figure 5.1: (a) Plot of growth rate exponent *n* versus isothermal annealing time *t* for oxidation of $MoSi_2B$-6 wt% Al and $MoSi_2B$-12 wt% Al in pure Argon (black axis, vertical line for *n* of oxidation in Argon represents the 3 different experiments) and CO/CO_2 (blue axis, bold-solid line). (b) Logarithmic plot of mass gain for 48h TG/m_o for $MoSi_2B$-6 wt% Al and $MoSi_2B$-12 wt% Al oxidation in CO/CO_2. (c) Initial stage (0-1 hour) for $MoSi_2B$-6 wt% Al and $MoSi_2B$-12 wt% Al oxidation in pure argon and CO/CO_2.

In the initial oxidation stage, an oxide scale is not present and thus the surface reaction between particles/gas controls the oxide growth rate. This is denoted by linear growth kinetics for oxidation in both Argon and CO/CO_2 (see **Figure 5.1**(c)). The goodness of fit R^2 of logarithmic plot at the initial stage is slightly smaller than the following oxidation stage. This suggests that the initial oxidation stage in CO/CO_2 is described with the combination of linear and logarithmic rate law. According to mass-gain curve in **Figure 4.4**, oxidation in Argon leads to a higher mass gain for $MoSi_2B$-6 wt% Al compared to $MoSi_2B$-12 wt% Al due to simultaneous oxidation of Al and Si in the initial oxidation stage. Oxidation with CO/CO_2 shows more mass-gain than in pure Argon due to more alumina formation.

Therefore, oxidation in low pO_2 favours the selective Al oxidation and prevents simultaneous oxidation of Al and Si. This suggests higher mass gain of $MoSi_2B$-12 wt% Al than in $MoSi_2B$-6 wt% Al caused by the higher fraction of $Mo(Al_x,Si_{1-x})_2$ hexagonal C40 constituting the particles.

5.1.2 Composition and phases of the healing particles

Based on real Al content analysed with EPMA of many particles (see **Table 4.3**), the composition for starting $MoSi_2B$-6 wt% Al and $MoSi_2B$-12 wt% Al particles is much lower than the nominal composition. There is $4.1^{+4.0}_{-1.5}$ wt% Al for $MoSi_2B$-12 wt% Al and the composition lies in a three-phases region of $Mo(Al_x,Si_{1-x})_2$ hexagonal C40 + $MoSi_2$ tetragonal $C11_b$ + Mo_5Si_3 D8m (see **Figure 5.2**). On the contrary, $MoSi_2B$-6 wt% Al with $2.7^{+13.7}_{-1.6}$ wt% Al, is in a two-phases region of $MoSi_2$ tetragonal $C11_b$ + Mo_5Si_3 D8m. This analysis is in good agreement with XRD results of the starting powders (**Figure 4.2**).

According to the EPMA analysis of Mo-B region inside the particles (see Mo-B region in **Figure 4.13**), the Mo-B phases are found but also accompanied with varying Si and O. Mole fraction of Mo:Si:B in $MoSi_2B$ ($MoSi_2$ + 2 wt% B) alloy is 32,7 : 9,0 : 58,3. In $Mo(Al_x,Si_{1-x})_2$ system, Al substitutes Si thus mole fraction of Si is lower than 58.3. This composition lies between two three-phases regions ($MoSi_2$-MoB-Mo_5Si_3 and $MoSi_2$-MoB-Mo_2B_5) as shown in phase diagram of Mo-Si-B system (**Figure 2.2**). This suggests the phases present in Mo-B region are constituted with complex co-existence of all these phases. In addition, trapped oxygen during embedding the particles in copper polymer might be the reason of observed O during EPMA investigation.

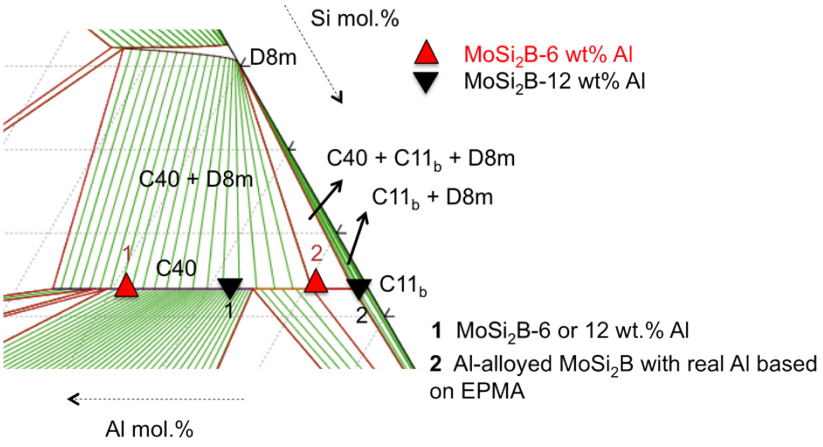

Figure 5.2: Plotting of composition in Mo-Si-Al phase diagram for $MoSi_2B$-6 and 12 wt% Al. Phase diagram was calculated with ThermoCalc based on the study by Turchi et al.[53].

There are shifting of diffraction lines for hexagonal C40 and tetragonal $C11_b$ between starting $MoSi_2B$-6 wt% Al and $MoSi_2B$-12 wt% Al powders (see **Figure 4.2** for the XRD results). In addition, the diffraction lines of these phases are also shifted between starting powders and after oxidation treatment; see **Figure 5.3**. This denotes the change of lattice parameters of hexagonal C40 and tetragonal $C11_b$ due to the variation of Al content as confirmed by Tabaru et al[49]. Besides this diffraction lines shifting, growth of $MoSi_2$ tetragonal $C11_b$ and loss of $Mo(Al_x,Si_{1-x})_2$ hexagonal C40 (see **Table 4.4**) also suggest that Al is depleted from these phases during the oxidation. This is in agreement with observation by SEM (**Figure 4.9** and **Figure 4.10**) where rich Al_2O_3 is the main forming oxide.

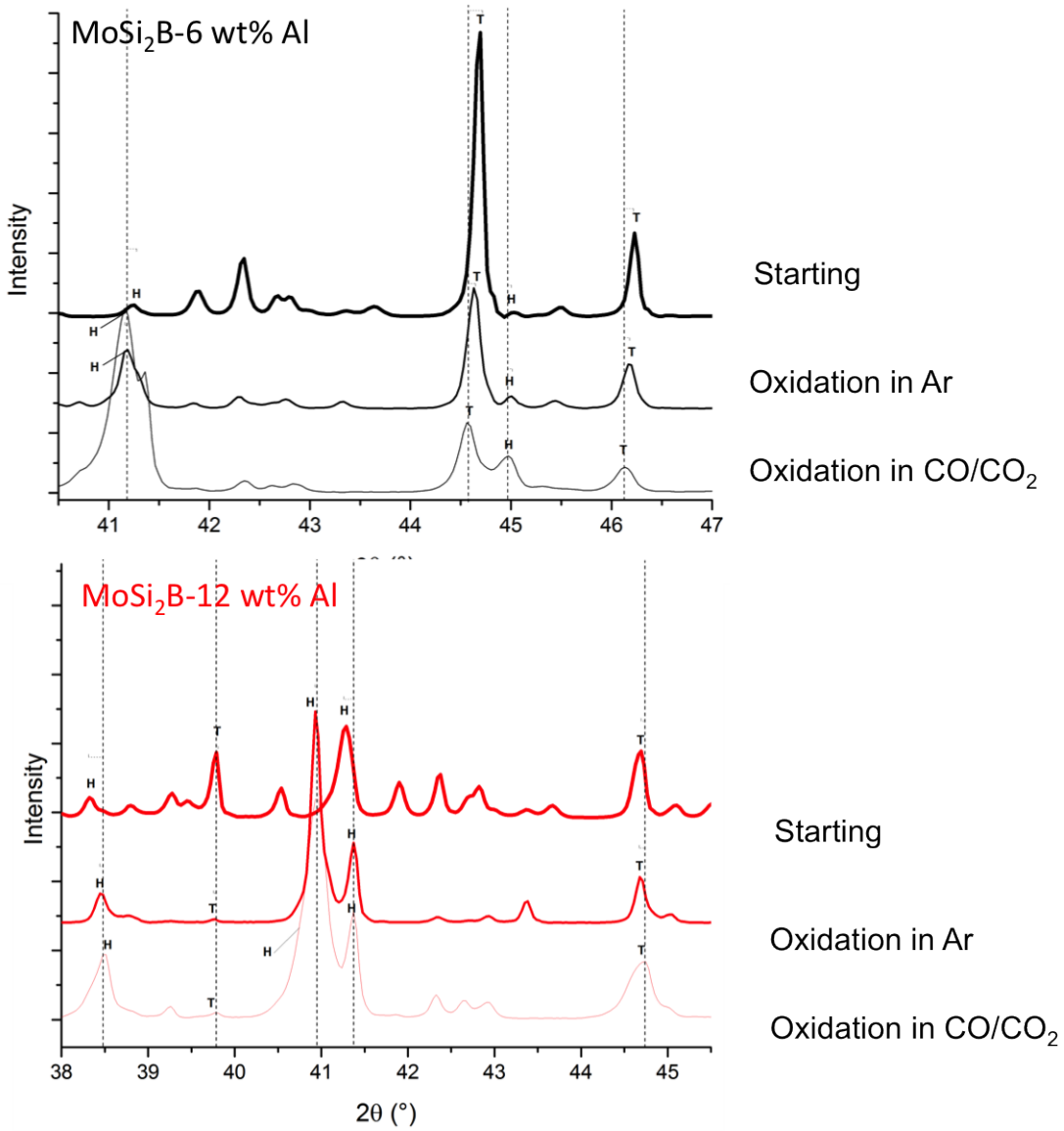

Figure 5.3: XRD results showing the shifting between $Mo(Si_{1-x},Al_x)_2$ C40 and $MoSi_2$ tetragonal $C11_b$ between starting powders and after oxidation in TGA for $MoSi_2B$-6 wt% Al (top) and $MoSi_2B$-12 wt% Al (bottom).

5.1.3 Oxide formation

As mentioned before, more alumina was formed after oxidation in CO/CO_2 compared to after oxidation in pure Argon. However, measurement with Rietveld refinement shows slightly lower amount of alumina (see **Table A.2.1**) after oxidation in CO/CO_2. This might be caused by reaction between the alumina and B_2O_3 forming Aluminium borate during the initial oxidation stage. According to measurement with Rietveld refinement, carburisation of the particles resulted in carbide formation with 1.83-2.78 wt% of Mo_2C (ρ = 8.9 gr/cm^3) and 1.36-3.89 wt% of $Mo_{4.8}Si_3C_{0.6}$ (ρ = 8.2 gr/cm^3). Beside these carbides, Mo (ρ = 10.28 gr/cm^3, see **Figure 4.6** for the XRD result) and excess of B_2O_3 might also form as the by-product of the carburisation of the particles. The disappearance as well as change of intensity of few diffraction lines corresponding to the Mo-B peaks i.e. MoB_2 and Mo_2B_5 after oxidation (**Figure 4.5** and **Figure 4.6**) suggests the formation of B_2O_3 and this oxide together with alumina forms Aluminium borate. Therefore, in addition to more exclusive alumina formation via selective oxidation of Al, the formation of high-mass density of carbides might be also the cause of higher mass gain in CO/CO_2 compared to oxidation in pure Argon.

Alumina is thermodynamically more favoured to form than silica due to its low Gibbs free energy (see **Table B.3.1**) i.e. at > 1000 °C. However simultaneous oxidation of Al and Si can occur due to inhomogeneity of $Mo(Al_x,Si_{1-x})_2$ hexagonal C40 distribution among particles. Si is also started to oxidise if the phases with lower Al content e.g. Mo_5Si_3, Mo-B or $MoSi_2$ were present instead of $Mo(Al_x,Si_{1-x})_2$. This prevents protective alumina shell to form and thus Si can be easily oxidised. If Al is completely depleted from $Mo(Al_x,Si_{1-x})_2$ e.g. after low pO_2 annealing process, Si is also then oxidised. Low-viscosity a-SiO_2 can also penetrate Al_2O_3 followed by the dissolution of Al_2O_3 according to the study of mullite formation from α-Al_2O_3/a-SiO_2 coupling[62, 63]. Toshio et al. also suggested that the dissolution of alumina into silica occurred at T=1863 K through the substitution of Al^{3+} ion to Si^{4+}[64]. Diffusion of the metal cation Al^{3+} or Si^{4+} through the oxide was faster due to the small amount of oxygen and therefore new oxide formed towards oxide/gas interface with whisker morphology (see **Figure 4.7**-**Figure 4.10**). Moreover, Aluminium borate[65] and mullite[66] also inherits whisker morphology. Mullite phase exist in different ratio of Al_2O_3:SiO_2 ranging from 1:1, 2:1 and 3:1[67]. According to literature, mullite scale or particles in the oxide was indeed observed when oxidizing bulk $Mo(Si,Al)_2$ alloys however only after long oxidation in air atmosphere[30, 51, 52, 68]. In our experiment, mullite was not observed by XRD. This suggests mullite was not formed due to the mild oxidizing conditions in Argon or CO/CO_2.

5.2 In situ encapsulation

5.2.1 Mechanism of in situ encapsulation

Theoretical alumina shell thickness δ can be calculated by assuming the particle is perfectly spherical and only composed of $Mo(Al_x,Si_{1-x})_2$ hexagonal C40 according to:

$$\delta = r_{particle}\left(\left(1+\frac{X\ wt.\%\ Al}{2}\frac{Mr_{alumina}\rho_{particle}}{\rho_{alumina}\ Ar_{Al}}\right)^{1/3}-1\right) \quad \textbf{(5.4)}$$

With $r_{particle}$ (µm) is taken from D[50] in **Table 4.1**, x is the wt% Al in the starting alloy and is taken from real Al content in **Table 4.3** and assuming $\rho_{particle} \approx \rho_{MoSi_2}$. If Al is completely depleted from $Mo(Al_x,Si_{1-x})_2$, the optimum alumina shell thickness δ for $MoSi_2$B-6 wt% Al and $MoSi_2$B-12 wt% Al are 0.40 µm and 0.69 µm, respectively. Referring to Al depletion from SEM/EDS and EPMA (see **Table 4.5** for the Al content after SPS and after low pO_2 annealing), the theoretical alumina shell thickness and the measured thickness from SEM images can be compared as well. After SPS, the theoretical alumina shell thickness is about 0.22 µm for $MoSi_2$B-6 wt% Al and 0.38 µm for $MoSi_2$B-12 wt% Al particle. Whereas after low pO_2 annealing for 16 hours at 1100 °C in pure Argon, the thickness for $MoSi_2$B-6 wt% Al is 0.38 µm and for $MoSi_2$B-12 wt% Al is 0.52 µm. The discrepancy between theoretical and measured scale thickness is due to the particle shape irregularity and inhomogeneous distribution of $Mo(Al_x,Si_{1-x})_2$ hexagonal C40 which eventually resulted in simultaneous oxidation of Al and Si.

Figure 5.4 shows the schematic for shell development around $MoSi_2$B-6 wt% Al particles in the composite. Other than $Mo(Al_x,Si_{1-x})_2$, phases such as $MoSi_2$, Mo_5Si_3 and Mo-B phase are also present in the starting particle. The region with $Mo(Al_x,Si_{1-x})_2$ creates uniform layer of alumina shell. However except $MoSi_2$B-12 wt% Al particles, $MoSi_2$B-2 wt% Al and $MoSi_2$B-6 wt% Al particles contain also a large fraction of $MoSi_2$ tetragonal $C11_b$ with no Al content. Thus the region with this low Al content (e.g. tetragonal $C11_b$, Mo_5Si_3 and Mo-B phases) forms very limited alumina shell. The formation of Mo_5Si_3 underneath alumina shell is provided by the rapid oxidation of Al from $Mo(Al_x,Si_{1-x})_2$ phase. Thicker Mo_5Si_3 in the case of YSZ+10MSB12A composite is in agreement with the study from Ramberg et al[51]. Ramberg et al. found that Mo_5Si_3 formed only for $Mo(Al_{0.1},Si_{0.9})_2$ and did not form for $Mo(Al_{0.01},Si_{0.99})_2$. The particles with less Al such as $MoSi_2$B-2 wt% Al then formed very thin Mo_5Si_3 underneath the shell because of the oxidation of slow Si instead of Al at this high temperature[43]. Mo_5Si_3 is also formed according to $\frac{5}{7}MoSi_2 + O_2 \rightarrow \frac{1}{7}Mo_5Si_3 + SiO_2$ and may be followed by $2Mo_5Si_3 +$

$21O_2 \rightarrow 10MoO_3 + 6SiO_2$ [69] if Si is also oxidised. Mo_5Si_3 formation is accompanied by volume expansion, creating irregularity between particle/shell interfaces. MoO_3 does not form due to the low pO_2 at oxide/particle interface, which also not formed according to the TGA study of the particles.

After low pO_2 annealing, the shell becomes thicker either with previously alumina growth or newly formed silica. Simultaneous oxidation of Al and Si occurred if there is no alumina shell protection and also if the phases are consisted with no Al i.e. Mo_5Si_3 and Mo-B phase, or if the Al is already depleted. Furthermore, mixed alumina-silica can form when a-SiO_2 dissolute Al_2O_3 or formed via Al^{3+}-Si^{4+} substitution (cf. **Section 5.1.3**). Subsequently, Si^{4+} diffusion to zirconia initiated the zircon formation. If the shell is not protective, the particles may be fully oxidised to silica.

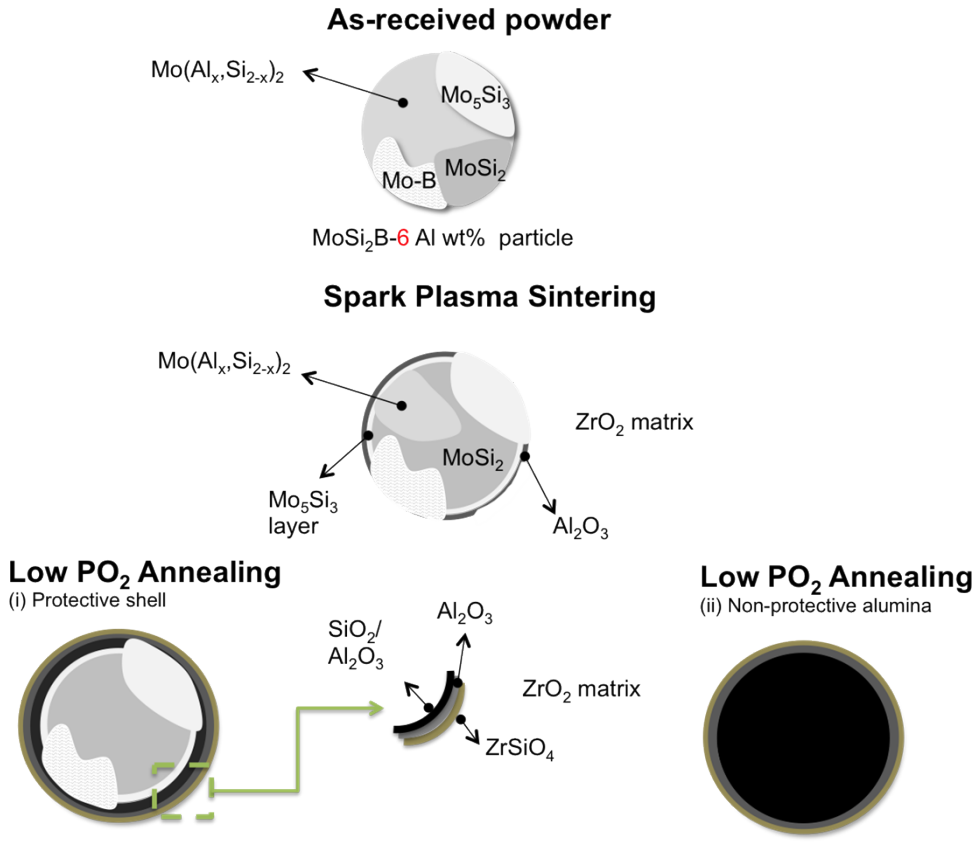

Figure 5.4: Schematic of alumina shell formation around $MoSi_2B$ particles in YSZ + $MoSi_2B$-6 wt% Al (YSZ+10MSB6A) composite.

After in situ encapsulation of the composite via low pO_2 annealing in pure Argon, the shell composition is in agreement with oxide composition of Al-alloyed $MoSi_2B$ particles after TGA in pure Argon: mixed Al_2O_3-SiO_2 for $MoSi_2B$-6 wt% Al and more exclusive alumina for

$MoSi_2B$-12 wt% Al. However, the formation of silica and zircon shell for particles in YSZ+10MSB12A composite annealed in CO/CO_2 with pO_2 = 9.1 x 10^{-14} atm is conflicting with the TGA result. In the same oxidising condition, more exclusive alumina shell was formed around $MoSi_2B$-12 wt% Al particles. Whereas silica is also formed for the same particles in the presence of YSZ matrix. Therefore exclusive alumina formation in the composite was not achieved as in the case of oxidation of Al-alloyed $MoSi_2B$ powders in lower pO_2 by CO/CO_2.

5.2.2 Oxygen source

The SPS process took place at high temperature (1200 °C) under inert Argon and also reducing atmosphere created by the graphite (mold, punch and paper, see **Figure 3.1** for the schematic of SPS). Alumina formation in this atmosphere was thus not expected (see **Figure 4.12**). Entrapped oxygen may be the cause for this oxidation in inert/reducing atmosphere. Another possibility is also oxidation-reduction reaction of Al-alloyed $MoSi_2B$ particles with zirconia matrix. The oxidation-reduction reaction is not spontaneous since zirconia is a more stable oxide compared to alumina and silica (see **Table B.3.1** for the calculation of dissociation pO_2 of oxide). However, Li et al. found oxidation of titanium accompanied with darkening and partially reduced zirconia ZrO_{2-x} after joining titanium-containing brazing materials with ceramics in low pO_2 environment (vacuum ~ $pO_2<10^{-6}$ atm)[70-72]. The formation of in situ thermally growth oxide (TGO) as aluminium oxide in an inert atmosphere also suggested the partial reduction of YSZ in the case of TBC fabrication with SPS[73-75]. Song et al. also observed the darkening of 7YSZ top-coat post-sintering process as a result from partial reduction of zirconia with formation of alumina from Al foil[76]. Anselmi-Tamburini et al. associated the darkening of YSZ after SPS with the occurrence of oxygen non-stoichiometry via partial reduction of the zirconia[77]. All YSZ+10MSBA composites were dark-grey after the SPS process, which therefore suggests that the partial reduction of zirconia may play a role in oxidising the particles.

According to the Brouwer diagram of pure zirconia (**Figure 5.5**), types of dominating defects may be changed under the non-equilibrium condition. In low pO_2 atmosphere, the predominant defects are oxygen vacancies which are compensated by electron $n = 2[V\ddot{o}]$. The relationship in equilibrium condition is,

$$n = (2K_1)^{\frac{1}{3}} PO_2^{\ -\frac{1}{6}} \quad \textbf{(5.5)}$$

The evolution of oxygen vacancy $[V\ddot{o}]$ according to Equation **(5.5)** is succeeding the decomposition of oxygen from the lattice O_O^x[78, 79]:

$$O_O^x \leftrightarrow \frac{1}{2}O_2 + V\ddot{o} + 2e' \quad \textbf{(5.6)}$$

According to the study of YSZ membrane with pO_2 gradient ranging from 0 to 10^{-9} atm between feed and permeate side, the oxygen flux in 1 mm YSZ thickness at high temperature was of the magnitude of $J_{O_2} \approx 10^{-8}\, mol.cm^{-2}s^{-1}$ [80]. With thicker YSZ, the oxygen flux is lowered even more. However after low pO_2 annealing, the shell of the particles near the surface and towards the centre of the composite did not show any difference. Therefore, zirconia matrix may also play role in alumina formation during this stage. The presence of mixed alumina-silica shell in YSZ+10MSB12A composite also indicated the role of zirconia in oxidising the particles after annealing in lower pO_2 using CO/CO_2.

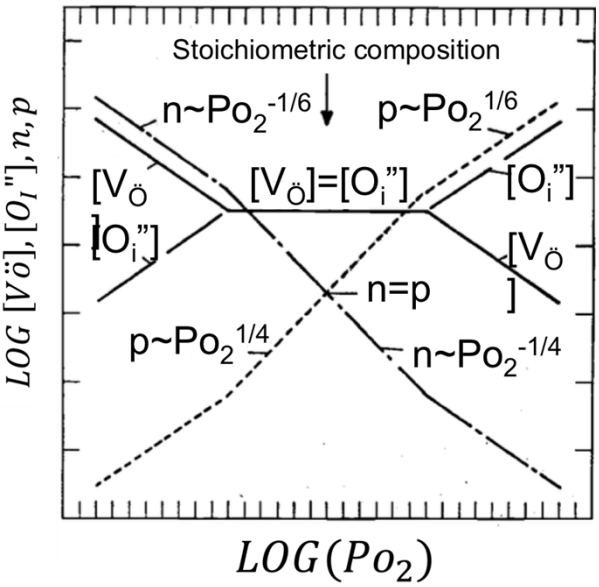

Figure 5.5: Brouwer diagram for pure zirconia[81] . $[V\ddot{o}]$ and $[O_i"]$ denote the Krōger-Vink notation for oxygen vacancies and interstitial oxygen, respectively.

5.2.3 Zirconia matrix decomposition

Observed cracks at outer side/yellow region of the composite (see **Figure 4.17**) after 100 hours annealing in open air are probably caused by the zirconia decomposition via martensitic transformation from t-ZrO_2 to m-ZrO_2. The surface of the sample was not perfectly free of micro-cracks from the surface preparation. These micro-cracks acted as high-diffusivity paths for oxygen and in the end it resulted in accelerated oxidation of

particles near the surface. The oxide formation was accompanied with stress to the surrounding and cracks eventually appeared. In addition, other than the stable phases of zirconia, metastable t'-ZrO_2 may be formed as well e.g. after rapid cooling[57]. This phase can decompose to high (c-ZrO_2) and low yttria (m-ZrO_2 and t-ZrO_2) domain due to Yttria segregation[58, 79]. The martensitic transformation via t-ZrO_2 ↔ m-ZrO_2 exerted volume change and eventually cracks may be initiated in the outer side. The difference of oxygen and temperature exposure between the inner side (dark-grey) and outer side (yellow) region of the composite resulted in different stable phase between the two. According to Ho et al., the colour change to ivory/yellow due denotes the stoichiometry recovery of ZrO_{2-x}[77, 79]. During the cooling, the volume expansion between the two regions resulted in crack between them the inner side (dark-grey region) and outer side (yellow region). Nevertheless, even after severe oxidation in the yellow region, few particles were still intact showing the protection by alumina shell.

5.3 Mechanism of crack-gap filling

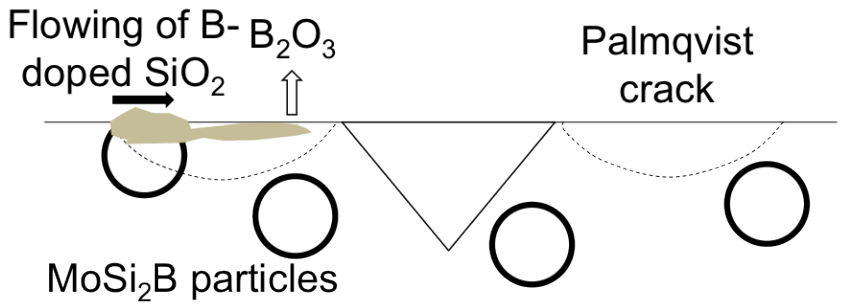

Figure 5.6: The schematic of healing in YSZ + $MoSi_2B$-6 wt% Al (YSZ+10MSB6A) composite.

The irregularity of particle/oxide interface caused by Mo_5Si_3 formation result in weak region between particle/oxide where often cracks were deflected to this interface (see **Figure 4.19**). Nevertheless, the attraction of crack to the particle is beneficial for crack healing. **Figure 5.6** shows the mechanism of crack gap filling in YSZ+10MSB6A composite. During healing treatment in air, reaction $\frac{5}{7}MoSi_2 + O_2 \rightarrow \frac{1}{7}Mo_5Si_3 + SiO_2$ and $2Mo_5Si_3 + 21O_2 \rightarrow 10MoO_3 + 6SiO_2$ takes place. At high temperature, MoO_3 was volatilised due to the high pO_2 in air. The formed amorphous silica flows through the crack and reacts with zirconia matrix to form zircon $ZrSiO_4$. Visually, the cracks were filled with 50% success rate. Healing product was consisted of silica, while no zircon inside the crack-gap was formed. Al may be present inside the healing product due to the present $Mo(Si_{1-x},Al_x)_2$ phase. Dissolved alumina inside

the amorphous silica may change the viscosity[82] and ultimately affect the crack-gap filling successful rate.

There are two possible reasons for the unfilled crack-gap: B_2O_3 volatilisation and small crack-gap. According to other study, B is easily volatilised to B_2O_3[83] which ultimately may reduce the flow ability of amorphous silica. Nevertheless, zircon was sometimes observed around the crack, proving the flow ability of B-doped SiO_2 inside the crack gap. Oxides sometimes did not fill crack also due to small cracks and further the crack narrowing during the healing treatment. Thus the oxide may tend to go to the surface instead of filling the crack-gap. The EDS analysis was not accurate since the oxide usually located inside the crack-gap. In order to observe clearly the chemical composition of the filled crack, larger and more controlled cracks are required.

6

Conclusions and Recommendations

1.1 Conclusions

Oxidation kinetics:

Two healing particles with different Al composition were analysed with TGA: $MoSi_2B$-6 wt% Al and $MoSi_2B$-12 wt% Al in Argon and also CO/CO_2 with ratio of 4.2 at 1100 °C for 48h.

- Mixed Al_2O_3-SiO_2 oxide in $MoSi_2B$-6 wt% Al occurred during oxidation under Argon due to the shape irregularity and inhomogeneity distribution of $Mo(Al_x,Si_{1-x})_2$ hexagonal C40 while alumina was formed more exclusively with $MoSi_2B$-12 wt% Al . Oxidation of $MoSi_2B$-6 wt% Al and $MoSi_2B$-12 wt% Al particles in pure Argon at 1100 °C showed linear oxide growth rate kinetics at the initial oxidation stage followed by parabolic oxide growth rate kinetics.

- An alumina shell was exclusively formed after oxidation of $MoSi_2B$-6 wt% Al and $MoSi_2B$-12 wt% Al under CO/CO_2 with a ratio of 4.2 due to the lower pO_2. Oxidation of $MoSi_2B$-6 wt% Al and $MoSi_2B$-12 wt% Al particles in CO/CO_2 of 4.2 showed linear + parabolic oxide growth rate kinetics in the initial oxidation stage followed by logarithmic oxide growth kinetics.

In situ encapsulation of $MoSi_2B$ particles:

Three composites were prepared to study the in situ alumina formation around the particles: YSZ+10MSB2A (YSZ matrix + $MoSi_2B$-2 wt% Al particles), YSZ+10MSB6A (YSZ matrix + $MoSi_2B$-6 wt% Al particles), and YSZ+10MSB12A (YSZ matrix + $MoSi_2B$-12 wt% Al particles). Low pO_2 annealing in pure Argon and also CO/CO_2 with a ratio of 4.2 at 1100 °C for 16 hours was conducted to thicken the shell encapsulation.

- After low pO_2 annealing in pure Argon, particles in YSZ+10MSB12A formed alumina more exclusively while in YSZ+10MSB2A and YSZ+10MSB6A composite was composed of

alumina and silica mixture denoting the lack of Al content inside the particles. Nevertheless all particles showed protection during the exposure of composite in air at 1100 °C for 100 hours.

- Low pO_2 annealing with CO/CO_2 with ratio of 4.2 (pO_2 = 9.1 x 10^{-14} atm) showed simultaneous oxidation of Al and Si even for the particles in YSZ+10MSB12A composite. This suggested that oxygen source during low pO_2 annealing in Argon or CO/CO_2 came from the zirconia matrix as well. Annealing the composite in inert/reducing atmosphere promoted $V\ddot{o}$ allowing non-stoichiometry of zirconia ZrO_{2-x} and eventually partially reduced zirconia to establish through oxygen decomposition from zirconia lattice.

Crack-gap filling:

Two samples were analysed for the crack-gap filling experiment: YSZ+10MSB6A with pre-encapsulated healing particles and in situ encapsulated healing particles. The healing treatment was done by exposing the composite at 1100°C in laboratory air for 1, 4 and 16 hours.

- Silica filled the crack made by Vickers indentation about 50% success rate with no difference between all samples. There are two possible reasons for unfilled crack-gap. First, B_2O_3 may be volatilised reducing the flow ability of amorphous silica. Second, small crack-gap from Vickers indentation and even narrower crack-gap after healing may also prevent silica to fill the crack-gap.

1.2 Recommendations for future work

The following recommendations are proposed in order to get more understanding of the in situ encapsulation of the particles:

- TGA study of $MoSi_2B$ particles to validate the selective oxidation of Al and to validate the kinetics of silica or borosilicate formation in pure Argon and CO/CO_2 with ratio of 4.2.
- Creating particles with more homogeneous $Mo(Si_{1-x},Al_x)_2$ hexagonal C40 by alloying Al to the composition of two phases region $Mo(Si_{1-x},Al_x)_2$ hexagonal C40 + Mo_5Si_3 D8m (from 5-30 mol% Al). For this this composition the $MoSi_2$ tetragonal $C11_b$ will be absent and therefore regardless of the shape inhomogeneity, selective oxidation of Al is still favoured.
- Creating larger and more controlled crack-gap to study the crack-gap filling composition and kinetics.

A

Result of Semi-quantitative Analysis using Rietveld Refinement

The weight-fraction semi-quantitative analysis for powders was conducted with Maud software by Java. The 2θ(°) from 0-35.5 was selected to minimise the fitting error caused by complex diffraction lines around 37-45°. As a result, free Mo (approximately at 41-42°) was not included in the measurement. R_{wp} stands for weighted profile R-factor where R_{wp} < 10% corresponded to good refinement[84, 85]. On the other hand, sigma is the goodness of fit and it is the ratio between R_{wp} and R_{exp} (R_{exp} is the expected or the best possible R_{wp}). Value of sigma lower than 2 denotes acceptably good refinement. High R_{wp} for $MoSi_2B$-12 wt% Al (TGA in pure Argon) was due to the few yet unidentified XRD peaks.

Table A.2.1: Weight fraction (wt%) of compounds analysed using Rietveld Refinement.

Compound (wt%)	Starting Powders		TGA in pure Argon		TGA in CO/CO_2 of 4.2	
	$MoSi_2B$-6 wt% Al	**$MoSi_2B$-12 wt% Al**	**$MoSi_2B$-6 wt% Al**	**$MoSi_2B$-12 wt% Al**	**$MoSi_2B$-6 wt% Al**	**$MoSi_2B$-12 wt% Al**
Tetragonal $C11_b$	18.9	3	48	0.8	62.3	22.1
Hexagonal C40	68.2	86.9	22.6	85.7	0.71	36.1
MoB	1.1	1.4	3.8	0.9	13.4	6.9
MoB_2	0.9	0.2	0	0	0	0
$MoB_{2.5}$	7.6	5.5	8.5	7.9		
$Al_{4.5}BO_{7.33}/AlBO_9$					10.7	20.6
Al_2O_3			14.5	2.9	7.2	1.1
Mo_2C					1.8	2.8
MoSiC					1.4	3.9
Al						
Si	3.2	3		2		
Mo_5Si_3			2.6	0.002	3.41	5.5
Rwp (%)	5.1	6.5	6.5	24.6	10.6	12.6
Sigma	0.6	0.8	0.6	1.1	0.9	1.1

B

Thermodynamic of Oxide Formation

The calculation of dissociation pO_2 for oxide (alumina, silica and zirconia) formation was done with assuming pure and immiscible oxide (activity $a_{oxide} \approx 1$). Gibbs free energy was obtained from Richardson-Ellingham diagram (i.e. see the diagram from this reference[61]). The activity of element $a_{Al} = \gamma_{Al} \cdot \chi_{Al}$ and $a_{Si} = \gamma_{Si} \cdot \chi_{Si}$ was also taken equal to its mole fraction with the assumption of $\gamma_{Al} = \gamma_{Si} = 1$. Yttria-stabilised zirconia was assumed as pure-zirconia and with the mole fraction of Zr according to crystal structure in **Figure 2.5**. The equilibrium constant *k* at fixed total pressure is as follows:

$$k = \exp\left(-\frac{\Delta G_f}{RT}\right) \qquad \textbf{(B.3.1)}$$

Table B.3.1: Dissociation pO_2 (atm) for oxides

Oxide	**Reaction**	ΔG_f **(kJ/1 mole O_2)**	**Dissociation pO_2 (atm)**
Al_2O_3	$\frac{4}{3}Al + O_2 \rightarrow \frac{2}{3}Al_2O_3$ χ_{Al}=11.25 mol% for $MoSi_2$B-6 wt% Al χ_{Al}=22.45 mol% for $MoSi_2$B-12 wt% Al	$-800\ kJ/mole$ (T = 1473 K)	$8.1.10^{-28}$ for $MoSi_2$B-6 wt% Al $3.1.10^{-28}$ for $MoSi_2$B-12 wt% Al
SiO_2	$Si + O_2 \rightarrow SiO_2$ χ_{Si} is 61.91 mol% Si in $MoSi_2$B-6 wt% Al	$-640\ kJ/mole$ (T = 1473 K)	$3.3\ x\ 10^{-23}$
	$\frac{5}{7}MoSi_2 + O_2(g) \rightarrow \frac{1}{7}Mo_5Si_3 + SiO_2$ $\Delta G_f(MoSi_2) \approx -116.5\ kJ$ [41] $\Delta G_f(Mo_5Si_3) \approx -333.8\ kJ$ [41] $\Delta G_f(SiO_2) \approx -640\ kJ/mole$		$5.9\ x\ 10^{-22}$
ZrO_2	$Zr + O_2 \rightarrow ZrO_2$ $\chi_{Zr} = 1.25$ mol% for yttria-stabilised zirconia	$-810\ kJ/mole$ (T = 1473 K)	10^{-30} 10^{-29}
CO_2	$2CO + O_2 \rightarrow CO_2$	$-310 kJ/mole$ (T = 1373 K)	9.1×10^{-14}

References

1. Clarke, D.R. and S.R. Phillpot, *Thermal Barrier Coating Materials.* Materialstoday, 2005. **8**(6): p. 8.
2. Padture, N.P., M. Gell, and E.H. Jordan, *Thermal Barrier Coatings for Gas-Turbine Engine Applications.* Science's Compass, 2002. **296**: p. 5.
3. Osada, T., et al., *Self-crack-healing behaviour in ceramic matrix composites*, in *Advances in Ceramic Matrix Composites*, I.M. Low, Editor. 2014, Woodhead Publishing Limited: Cambridge. p. 32.
4. Ghosh, S.K., *Self-healing materials: fundamentals, design strategies, and applications*. 2009, Weinheim: Wiley-VCH.
5. Ando, K., et al., *Crack-healing and mechanical behaviour of Al2O3/SiC composites at elevated temperature.* Fatigue and Fracture of Engineering Materials & Structures, 2004. **27**(7): p. 9.
6. Ando, K., et al., *Crack-healing Behaviour Under Stress of Mullite/Silicon Carbide Ceramics and the Resultant Fatigue Strength.* Journal of American Ceramic Society, 2001. **84**(9): p. 6.
7. Takahashi, K., et al., *Crack-healing behavior of Si3N4/SiC composite under stress and low oxygen pressure.* Materials Science and Engineering: A, 2009. **527**(15): p. 7.
8. Houjou, K., K. Ando, and K. Takahashi, *Crack-healing behaviour of ZrO2/SiC composite ceramics.* International Journal of Structural Integrity, 2010. **1**(1): p. 10.
9. Kilo, M., et al., *Oxygen Diffusion in Yttria Stabilised Zirconia - Experimental Results and Moleculra Dynamics Calculations.* Physical Chemistry Chemical Physics, 2003. **5**: p. 6.
10. Lommens, P., et al., *Synthesis and Thermal Expansion of ZrO2/ZrW2O8 Composites.* Journal of the European Ceramic Society, 2005. **25**(16): p. 6.
11. Sloof, W.G., et al., *Crack Healing in Yttria Stabilised Zirconia Thermal Barrier Coatings*, in *Self Healing Materials - Pioneering Research in the Netherlands*. 2015, IOS Press: The Netherlands. p. 219-227.
12. *Effective Elastic Modului of Alumina, Zirconia and Alumina-Zirconia Composite Ceramics*, in *Ceramics and Composite Materials: New Research*, B.M. Caruta, Editor. 2006, Nova Science Publishers, Inc.: New York.
13. Clarke, F.W., *Data of Geochemistry*. Vol. 695. 1920, Washington: Government Printing Office.
14. Mao, W., *Kinetics of Slef-Healing Reaction in TBC With MoSi2 Based Sacrificial Particles*, in *Materisl Science and Engineering*. 2013, TU Delft.
15. Rebillat, F., *Advances in self-healing ceramic matrix composites*, in *Advances in Ceramic Matrix Composites*, I.M. Low, Editor. 2014, Woodhead Publishing Limited: Cambridge. p. 41.
16. Méar, F.A., et al., *Self-Healing Process in Glassy Materials*, in *Self-Healing at The Nanoscale*, V. Amendola and M. Maneghetti, Editors. 2012, CRC Press Taylor & Francis Group: Florida. p. 260.
17. Balasubramanin, M., *Composite Materials and Procesing*. 2014, Florida: CRC Press Taylor & Francis Group.
18. Gao, L., et al., *Photoresponsive Self-Healing Polymer Composite with Photoabsorbing Hybrid Microcapsules.* Applied Materials & Interfaces, 2015. **7**: p. 7.
19. Heuer, A.H. and K.P.D. Lagerlof, *Oxygen Self-Diffusion in Corundum (alpha-Al2O3): A conundrum.* Philosophical Magazine Letters, 1999. **79**(8): p. 9.
20. Cuenca-Alvarez, R., et al., *The influence of dry particle coating parameters on thermal coatings properties*, in *Advanced Plasma Spray Applications*, H.S. Jazi, Editor. 2012, InTech. p. 250.
21. King, D.M., et al., *Atomic layer deposition on particles using a fluidized bed reactor with in sit spectrometry.* Surface and Coatings Technology, 2007. **201**(22-23): p. 9.
22. Kou, H.M., et al., *Al/Al2O3 Core-Shell Particles Synthesized by Wet-Chemical Based Route.* Key Engineering Materials: Composite Materials IV, 2006. **313**: p. 6.
23. Carabat, A.L., S.v.d. Zwaag, and W.G. Sloof, *Creating a Protective Shell for Reactive MoSi2 Particles in High-Temperature Ceramics.* Journal of the American Ceramic Society, 2015. **98**(8): p. 8.
24. Meijerink, M.J., *Coating of MoSi2 Healing Particles for Self-Healing Thermal Barrier Coatings*, in *Chemical Engineering*

Materials Science and Engineering. 2015, TU Delft: The Netherlands.
25. Paul, A., et al., *Development of Interdiffusion Zone in Different Systems*, in *Thermodynamics, Diffusion and The Kirkendall Effect in Solids*. 2014, Springer: London.
26. Kircher, T.A., *Engineering Limitations of MoSi2 Coatings.* Materials Science and Engineering: A, 1992. **155**(1-2): p. 8.
27. Knittel, S., S. Mathieu, and M. Vilasi, *The Oxiation Behaviour of Uniaxial Hot Pressed MoSi2 in Air from 400-1400 C.* Intermetallics, 2011. **19**(8): p. 9.

28. Liu, Y.Q., G. Shao, and P. Tsakiropoulos, *On The Oxidation Behaviour of MoSi2.* Intermetallics, 2001. **9**: p. 12.
29. Zhu, Y.T., et al., *Thermal Oxidation Kinetics of MoSi2-Based Powders.* Journal of The American Ceramic Society, 1999. **82**(10): p. 6.
30. Stergiou, A., P. Tsakiropoulos, and A. Brown, *The Intermediate and High-Temperature Oxidation Behaviour of Mo(Si1-xAlx)2 Intermetallic Alloys.* Intermetallics, 1996. **5**(1): p. 13.
31. Ingemarsson, L., et al., *Oxidation Behavior of a Mo(Si,Al)2 Composite at 900–1600 °C in dry air.* Journal of Materials Science, 2013. **48**(4): p. 13.
32. Sharif, A.A., *High-Temperature Oxidation of MoSi2.* Journal of Materials Science, 2010. **45**(4): p. 6.
33. Kriegel, M.J., et al., *Diffusion Path and Growth of Intermediate*
Phases in Mo/(Si,B) Diffusion Couples, in *18th Plansee Seminar 2013*. 2013: Austria.
34. Supatarawanich, V., D.R. Johnson, and C.T. Liu, *Effects of Microstructure on The Oxidation Behaviour of Multiphase Mo-Si-B Alloys.* Materials Science and Engineering: A, 2003. **344**: p. 12.
35. Ingemarsson, L., et al., *Oxidation Behaviour at 300-1000˚C of a (Mo,W)Si2-based Composite Containing Boride.* Intermetallics, 2010. **18**(1): p. 10.
36. Spreyer, R., *Thermal Analysis of Materials.* 1993: CRC Press.
37. Bach, H., F.K.G. Baucke, and D. Krause, *Eelctrochemistry of Solid Glasses*, in *Electrochemistry of Glasses and Glass Melts , including Glass Electrodes*, H. Bach, F.K.G. Baucke, and D. Krause, Editors. 2013, Springer-Verlag: Berlin.
38. Jozef, K., K. Róbert, and L. Marek, *High-Temperature Viscosity and Density of Alumino-Borosilicate Glasses as A Model System for Commercial E-Glass.* Ceramics-Silikáty, 2008. **52**(3): p. 7.
39. Ehrt, D. and R. Keding, *Electrical Conductivity and Viscosity of Borosilicate Glasses and Melts.* Physics and Chemistryi of Glasses-European Jounral of Glass Science and Technology Part B, 2009. **50**(3): p. 7.
40. Yanagihara, K., K. Przbylski, and T. Maruyama, *The Role of Microstructure on Pesting During Oxidation of MoSi2 and Mo(Si,Al)2 at 773 K.* Oxidation of Metals, 1997. **47**(3/4): p. 17.
41. Barin, I., *Thermochemical Data of Pure Substances.* 3rd Edition ed. 1995, Weinheim: VCH Verlagsgesellschaft mbH.
42. Maruyama, T., K. Yanagihara, and K. Nagata, 1993. **35**(5-8): p. 6.
43. Mitra, R., *Effect of Minor Alloying with Al on Oxidation Behaviour of MoSi2 at 1200 C.* Materials Science and Engineering: A, 1999. **260**(1-2): p. 15.
44. Fu, M. and J.A. Sekhar, *Processing, Microstructures, and Properties of Molybdenum Aluminosilicide.* Journal of The American Ceramic Society, 1998. **81**(12): p. 10.
45. Guo, C., et al., *A Thermodynamic Description of The Al-Mo-Si System.* Calphad, 2012. **36**.
46. Ponweiser, N., et al., *Phase Equilibria in the Al-Mo-Si System.* Intermetallics, 2011. **19**(3): p. 10.
47. Ramberg, C.E. and W.L. Worrell, *Fabrication and High-Temperature Phase Stability of Mo(Al,Si)2-MoSi2 Intermetallics.* Communications of the American Ceramic Society, 2000. **83**(4): p. 3.
48. Dasgupta, T., A.K. Bhattacharya, and A.M. Umarji, *Synthsis and Structure of Aluminum Subtituted MoSi2.* Solid State Communications, 2002. **126**(10): p. 6.
49. Tabaru, T., et al., *Effects of Subtitution of Al for Si on the Lattice Variations and Thermal Expansion of Mo(Si,Al)2.* Intermetallics, 2004. **12**(1): p. 9.
50. Tabaru, T., et al., *Influences of Al Content and Secondary Phases of Mo5(Si,Al3) on The Oxidation Resistance of Al-rich Mo(Si,Al)2-base Composites.* Intermetallics, 2003. **11**(7): p. 13.
51. Ramberg, C.E. and W.L. Worrell, *Oxidation Kinetics and Composite Scale Formation in the System Mo(Al,Si)2.* Journal of The American Ceramic Society, 2002. **85**(2): p. 9.
52. Ingemarsson, L., et al., *Oxidation Behaviour of a Mo(Si,Al)2 Based Composite at 1500C.* Intermetallics, 2011. **19**(9): p. 11.
53. Turchi, P.E.A. and A.I. Landa, *THERMODYNAMIC DATABASE, LOWER LENGTH SCALE, PART II:*
THERMODYNAMIC ASSESSMENT OF AL-MO-SI-U (M3MS-12LL0602092). 2012, Lawrence Livermore National Laboratory.
54. Minh, N.Q., *Ceramic Fuel Cells.* Journal of American Ceramic Society, 1993. **76**(3): p. 17.
55. Dudek, A., *Microstructure and Properties of The Composites: Hydroxyapatite with Addition of Zirconia Phase.* Journal of Engineering Materials and Technology, 2011. **133**(2): p. 5.
56. Chen, L.B., *Yttria-Stabilised Zirconia Thermal Barrier Coatings - A Review.* Surface Review and Letters, 2006. **13**(5): p. 10.
57. Limarga, A.M., et al., *Effect of high-temperature aging on the thermal conductivity of nanocrystalline tetragonal yttria-stabilized zirconia.* Acta Materialia, 2012. **60**(15): p. 18.
58. Witz, G., V. Shklover, and W. Steurer, *Phase Evolution in Yttria-Stabilized Zirconia Thermal Barrier Coatings Studied by Rietveld Refinement of X-Ray Powder Diffraction Patterns.* Journal of the American Ceramic Society, 2007. **90**(09): p. 6.

59. Song, G.M., et al., *High Temperature Oxidation Behaviour of Ti2AlC Ceramic at 1200°C.* Materials at High Temperature, 2012. **29**(3): p. 5.
60. Naumenko, D., et al., *Correlation Between the Microstructure, Growth Mechanism, and Growth Kinetics of Alumina Scales on a FeCrAlY Alloy.* Metallurgical and Materials Transactions A, 2007. **38**(12): p. 10.
61. Young, D.J., *High Temperature Oxidation and Corrosion of Metals*. 2016: Elsevier.
62. Li, N., et al., *A SImple and Efficient Way to Prepare Porous Mullite Matrix Ceramics via Directly Sintering SiO2-Al2O3 Microspheres.* Journal of The European Ceramic Society, 2016. **36**: p. 6.
63. Kleebe, H.-J., et al., *Conversion of Al2O3-SiO2 Powder Mixtures to 3:2 Mullite Following The Stable or Metastable Phase Diagram.* Journal of The European Ceramic Society, 2001. **21**(14): p. 13.
64. Maruyama, T., K. Yanagihara, and K. Nagata, *High Temperature Oxidation of Intermetallic Compounds of Mo(Si1-xAlx)2.* Corrosion Science, 1993. **35**(5-8): p. 6.
65. Li, J.X., et al., *In situ synthesis of porous ceramics with a framework structure of aluminium borate whisker.* Journal of Materials Science, 1998. **33**: p. 6.
66. Regiani, I., et al., *Nucleation and Growth of Mullite Whiskers from Lanthanum-Doped Aluminosilicate Melts.* Journal of American Ceramic Society, 2002. **85**(1): p. 7.
67. Schackelford, J.F. and R.H. Doremus, *Ceramic and Glass Materials: Structure, Properties and Processing*. 2008, New York: Springer Science+Business Media, LLC.
68. Maruyama, T. and K. Tanagihara, *High Temperature Oxidation and Pesting of Mo(Si,Al)2.* Materials Science and Engineering: A, 1997. **239-240**: p. 14.
69. Natesan, K. and S.C. Deevi, *Oxidation behaviour of molybdenum silicides and their composites.* Intermetallics, 2000. **8**(9-11): p. 12.
70. Lin, K.-L. and C.-C. Lin, *Reaction Between Titanium and Zirconia Powders During Sintering at 1500C.* Journal of American Society, 2007. **90**(7): p. 6.
71. Lin, K.-L. and C.-C. Lin, *Zirconia-Related Phases in the Zirconia/Titanium Diffusion Couple after Annealing at 1100° to 1550°C.* Journal of American Ceramic Society, 2005. **88**(10): p. 7.
72. Lin, K.-L., et al., *Interfacial and mechanical characterization of yttria-stabilized zirconia (YSZ) to stainless steel joints fabricated using Ag–Cu–Ti interlayers.* Ceramics International, 2007. **40**(1): p. 10.
73. Monceau, D., et al., *Pt-modified Ni aluminides, MCrAlY-base multilayer coatings and TBC systems fabricated by Spark Plasma Sintering for the protection of Ni-base superalloys.* Surface and Coatings Technology, 2009. **204**(6-7): p. 9.
74. Singh, M. and T.P. Shpargel, *Brazing of yttria-stabilized zirconia (YSZ) to stainless steel using Cu, Ag, and Ti-based brazes*. Journal of Materials Science, 2008. **43**: p. 10.
75. Boidot, M., et al., *Proto-TGO Formation in TBC Systems Fabricated by Spark Plasma Sintering.* Surface and Coatings Technology, 2010. **205**(5): p. 5.
76. Song, J., et al., *Simultaneous synthesis by spark plasma sintering of a thermal barrier coating system with a NiCrAlY bond coat.* Surface and Coatings Technology, 2010. **205**: p. 5.
77. Anselmi-Tamburini, U., et al., *Spark Plasma Sintering and Characterization of Bulk Nanostructured Fully Stabilized Zirconia: Part II. Characterization Studies.* Journal of Materials Research, 2004. **19**(11): p. 7.
78. Nowotny, J., T. Bak, and C.C. Sorrell, *Charge transfer at oxygen/zirconia interface at elevated temperatures: Part 4: Work function v. defect chemistry.* Advances in Applied Ceramics. Vol. 104. 2005. 7.
79. Ho, C.-J. and W.-H. Tuan, *Phase Stability and Microstructure Evolution of Yttria-Stabilized Zirconia during Firing in a Reducing Atmosphere.* Ceramics International, 2011. **37**(4): p. 8.
80. Park, H.J. and G.M. Choi, *The effect of surface coating on the oxygen permeation characteristics of zirconia.* Journal of the European Ceramic Society, 2005. **25**(12): p. 5.
81. Lee, T.A., *Dependence of Oxygen Vacancy Concentration in Zirconia on Processing Parameters and Reducing Conditions*, in *Physics*. 2000, Oregon State University.
82. Zhang, L. and S. Jahanshahi, *Modelling viscosity of alumina-containing silica melts.* Scandinavian Journal of Metallurgy, 2001. **30**: p. 6.
83. Yoshimi, K., et al., *Oxidation behavior of Mo5SiB2-based alloy at elevated temperatures.* Intermetallics, 2002. **10**(5): p. 8.
84. Toby, B.H., *R factors in Rietveld analysis: How good is good enough?* Powder Diffraction, 2006. **21**(1): p. 4.
85. Lutterotti, L., *Introduction to Diffraction and The Rietveld Method.*